4.1 Introduction

In this chapter the major features of development of prompt radiation fields and the shielding of these fields as they are produced at proton and ion accelerators are addressed. Particular emphasis is placed on the shielding of neutrons in view of their general dominance of the radiation fields. The shielding of muons at such accelerators is also described. Methods for utilizing the results of both semi-empirical and Monte Carlo methods in the solution of practical shielding problems are presented.

4.2 Radiation Production by Proton Accelerators

4.2.1 The Direct Beam; Radiation and Nuclear Interactions

Direct beams at proton accelerators, from the dosimetric standpoint, nearly always dominate over any type of secondary phenomena in terms of the level of hazard since the beam current is generally confined to small dimensions. Figure 1.4 gives the dose equivalent per fluence as a function of proton energy. The physical reason that the conversation factor shows such a prominent transition at about 200 MeV is that below that energy the proton range in tissue is less than the thickness of the human body. Hence as the energy is increased above 200 MeV, the energy largely escapes from the body so that it requires a far larger fluence of protons to deliver the same absorbed dose or dose equivalent.

The ionization range of a proton increases monotonically with energy. Since the mass of the proton is so much larger than that of the electron, the radiative processes of bremsstrahlung and synchrotron radiation are negligible at energies found at current accelerators. As will be discussed in Section 4.5, the cross sections for inelastic interactions become nearly independent of energy and have approximately the values tabulated in Table 1.2. Thus, as an individual proton passes through a material medium, the probability of it participating in an inelastic nuclear reaction before it loses its remaining energy to ionization becomes significant and, as the energy increases, becomes the dominant means by which protons are absorbed. Tesch has summarized this effect and the results are shown in Fig. 4.1 for various materials and energies (Te85).

4.2.2 Neutrons (and Other Hadrons at High Energies)

The production and behavior of neutrons at proton and ion accelerators have different characteristics as the energy is increased. The individual energy domains of proton energy, here denoted E_o will be discussed separately.

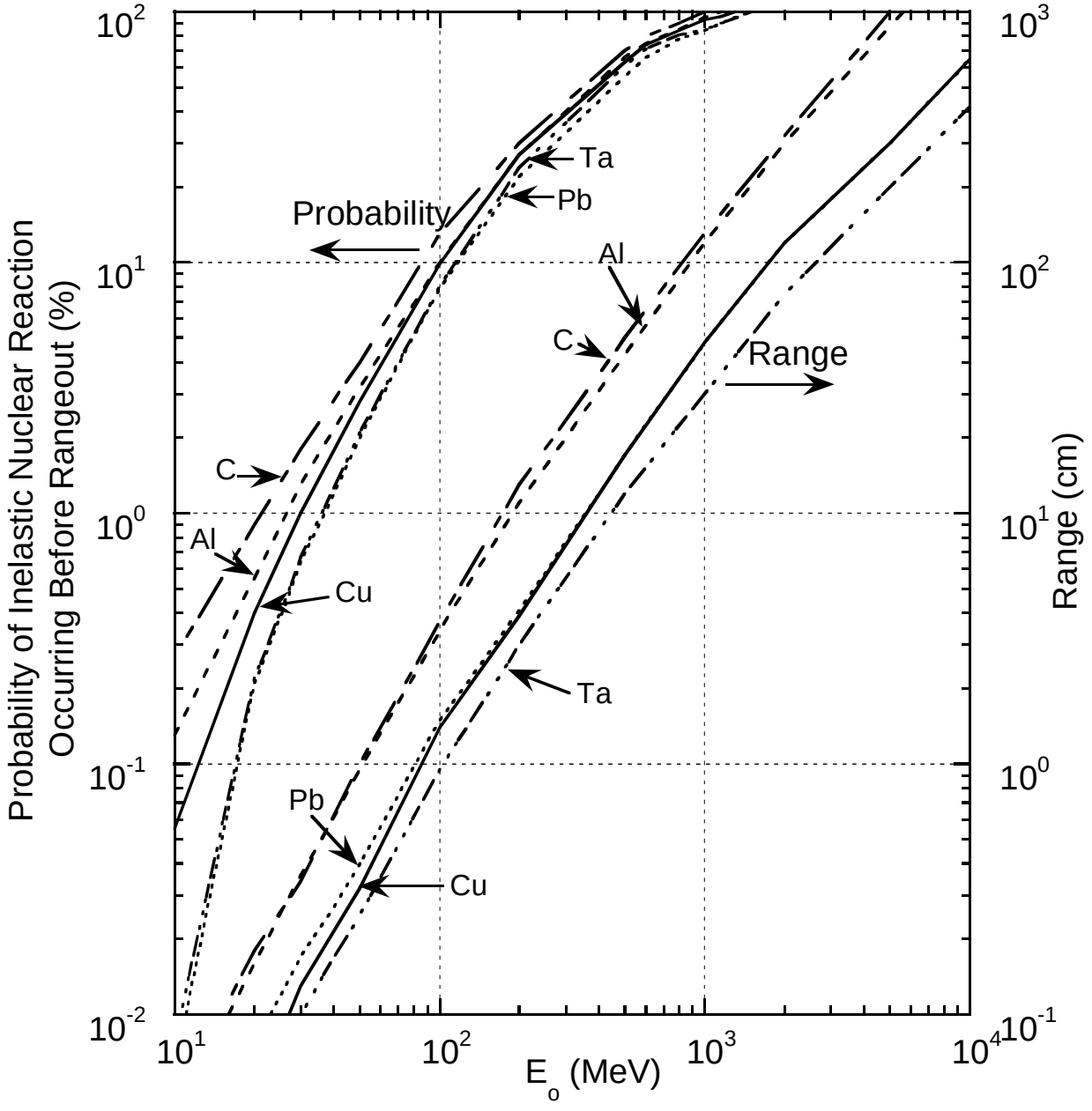

Fig. 4.1 Range of protons (**curves on right and right hand scale**) and probability of inelastic nuclear interaction within the range (**curves on left and left hand scale**) for various materials [Adapted from (Te85).]

4.2.2.1 E_o < 10 MeV

For a nuclear reaction, the **Q-value**, Q_v, is the energy released by the reaction and is defined in terms of the rest masses, m_i,

$$Q_v = [(m_1 + m_2) - (m_3 + m_4)]c^2, \tag{4.1}$$

for the nuclear reaction symbolized by $m_1 + m_2 \rightarrow m_3 + m_4$, alternatively denoted by $m_2(m_1,m_3)m_4$. Using the latter form of notation, the projectile is represented by m_1 while generally the less massive emitted particle is represented by m_3. $Q_v > 0$ implies an **exothermic** nuclear reaction. **Endothermic** ($Q_v \leq 0$) reactions are characterized by a **threshold energy**, E_{th} , given by

$$E_{th} = \frac{m_1 + m_2}{m_2}|Q_v|. \tag{4.2}$$

Below an kinetic energy of about 10 MeV, (p,n) reactions are important for some materials because these reactions commonly have very low threshold energies (E_{th} < 5 MeV). Many features are highly dependent upon the details of the structure of the target nuclei and are often sensitive to the target element, angle, and energy. For example, ^{7}Li(p,n)^{7}Be has a threshold energy of 1.9 MeV and a reaction cross section, σ, that quickly rises as a function of energy to a value of about 300 mb.

4.2.2.2 10 < E_o < 200 MeV

For protons having energies of this magnitude and higher, neutrons are usually the dominant feature of the radiation field that results from their interactions. In this region of energy, the yields are smoother functions of energy due to the lack of resonances, but are also more forward-peaked. Tesch (Te85) has summarized the total neutron yields, Y, per incident proton for different materials as a function of energy in Fig. 4.2. In this figure the smooth curves agree with the original primary data obtained from a myriad of experiments performed over several decades to within about a factor of two. An important feature is that for 50 < E_o < 500 MeV, $Y \propto E_o^2$ while for E_o > 1 GeV, $Y \propto E_o$. Especially at the lower energies, some of the neutrons produced are so-called **evaporation neutrons** that have an isotropic distribution due to the physical mechanism with which they are produced. Evaporation neutrons can be viewed as "boiling" off of a nucleus that has been "heated" by absorption of energy from the incident particle. Other neutrons that are produced are **cascade neutrons** that result directly from individual nuclear reactions. The latter are likely to have a directionality that can usually be described as at least mildly "forward-peaked". In this region there are extensive angular distribution data as a result of nuclear physics research. Representative examples of angular distributions of neutrons are given in Figs. 4.3 and 4.4 for 52 and 200 MeV protons, respectively.

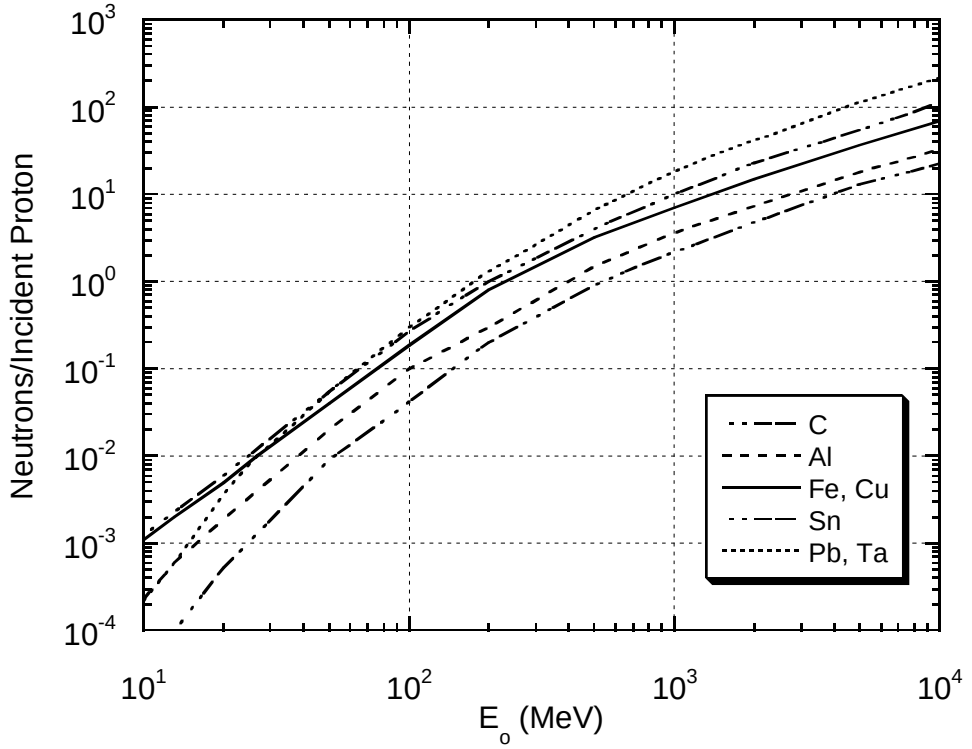

Fig. 4.2 Total neutron yield per proton for different target materials as a function of incident proton energy, E_o. [Adapted from (Te85).]

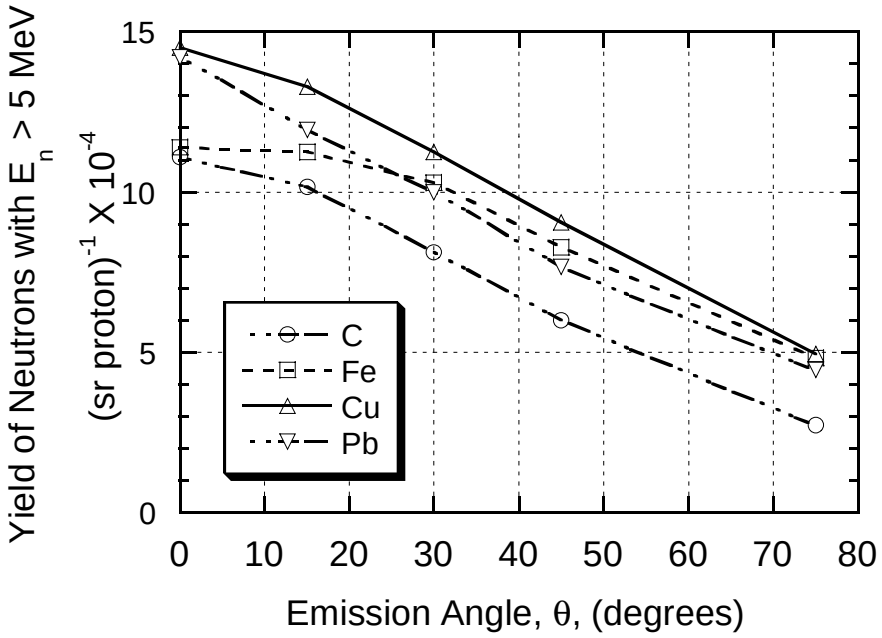

Fig. 4.3 Measured angular distributions of total neutron yield above 5 MeV for carbon, iron, copper, and lead bombarded by 52 MeV protons. The measurements were normalized at $\theta = 15^o$. The curves are drawn to guide the eye. [Adapted from (Na78).]

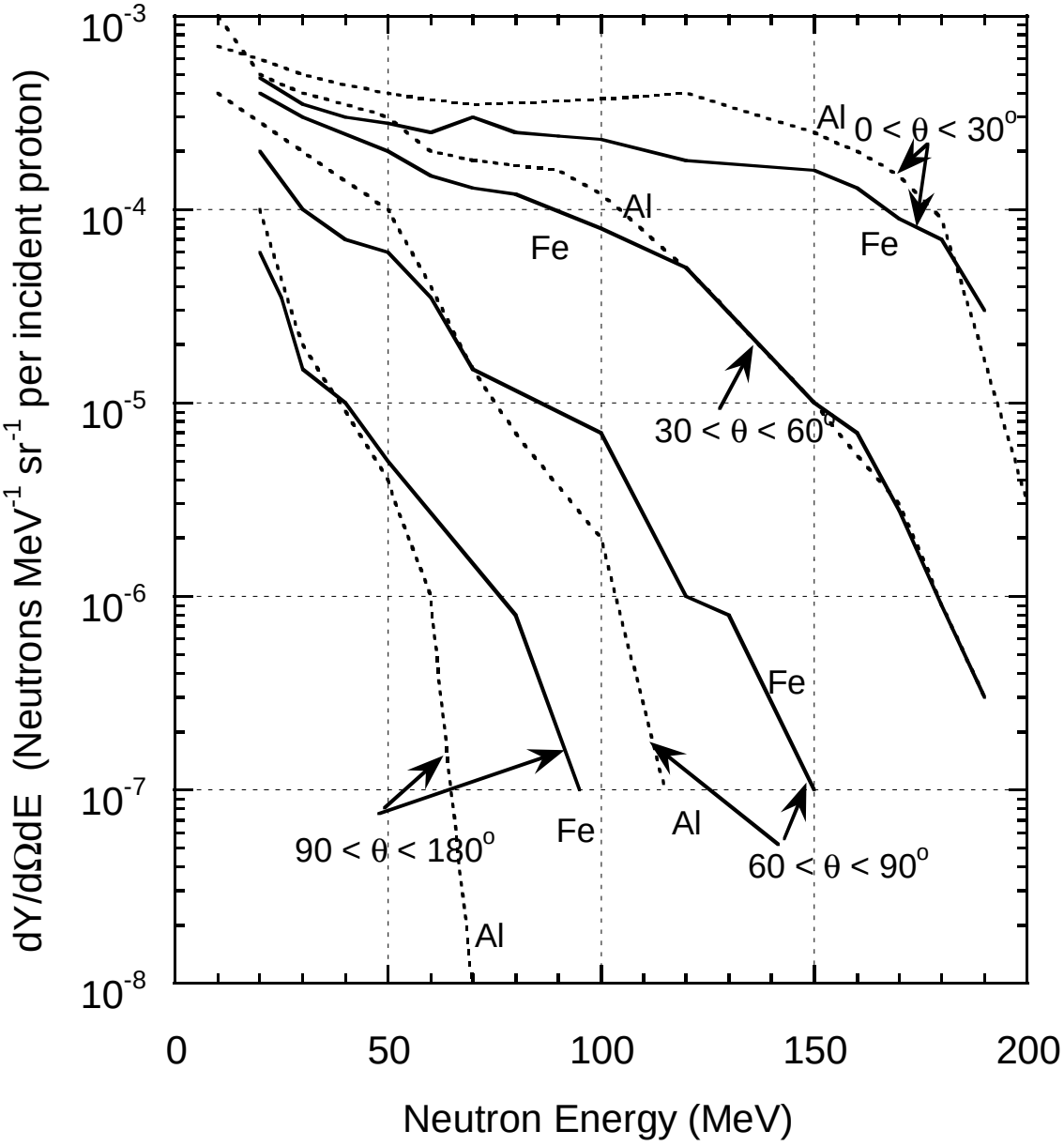

Fig. 4.4 Calculated energy spectra of neutrons emitted by iron and aluminum targets bombarded by 200 MeV protons for four ranges in θ. The iron calculations are from (Ha88) while the aluminum results are from (Al75). [Adapted from (Ha88).]

4.2.2.3 200 MeV < E_o < 1 GeV; ("Intermediate" Energy)

In this region, many more reaction channels become open and the number of protons emitted gradually becomes approximately equal to the number of neutrons. In fact, at the highest energies the radiation effects of protons and neutrons are essentially identical and both must be taken into account. Thus reliance on the values shown in Fig. 4.2 could underestimate radiation effects by as much as a factor of two. Also, at these energies, cascade neutrons become much more important than evaporation neutrons and thus the radiation field is more sharply forward-peaked with increasing primary particle energy.

4.2.2.4 E_O > 1 GeV ("High" Energy Region)

In this region, both the calculations and measurements become much more difficult. Often, "threshold" detectors are used to detect neutrons above some reaction threshold energy. This technique will be discussed at greater length in Section 9.5.3. Figures 4.5, 4.6, 4.7, and 4.8 show representative data at 14, 26, 22, and 225 GeV. These results should be regarded as **thin target** values. "Thin" target in this context means a target shorter than the **mean free path** for **removal** of the high energy protons. Table 4.1 summarizes common removal mean free paths. Considerable efforts have been made to semi-empirically fit the distributions of the yields of secondary particles produced by proton interactions. These efforts are needed to supply the needs of the particle physics community as well as to address radiation safety issues. They began in the early days of radiation protection and continue to the present and are embodied in the continual development of Monte Carlo programs designed to calculate the properties of hadronic cascades as discussed in Section 4.6. An example of a particularly successful early model is one developed by Ranft (Ra67) expressed as the following formula for the yield of protons (or neutrons):

$$\frac{d^2Y}{d\Omega dp} = \left\{\frac{A}{p_o} + \frac{Bp}{{p_o}^2}\left[1 + a\left\{1 - \frac{p_o}{p}\right\}\right]\right\} \times \left\{1 + a\left[1 - \frac{pp_o}{m^2}\right]\right\} p^2 \exp(-Cp^2\theta),$$

(protons or neutrons sr^{-1} GeV^{-1} per interacting proton) (4.3)

where

p_o is the primary proton momentum (GeV/c)
m is the proton rest energy (GeV/c^2)
$a = \{1 + (p_o/m)^2\}^{1/2}$
θ is the production angle (radians).

The parameters *A*, *B*, and *C* are material dependent and are given in Table 4.2.

When this formula is numerically integrated above the indicated particle threshold, it describes well the experimental data presented in Figs. 4.7 and 4.8, according to Patterson and Thomas (Pa73).

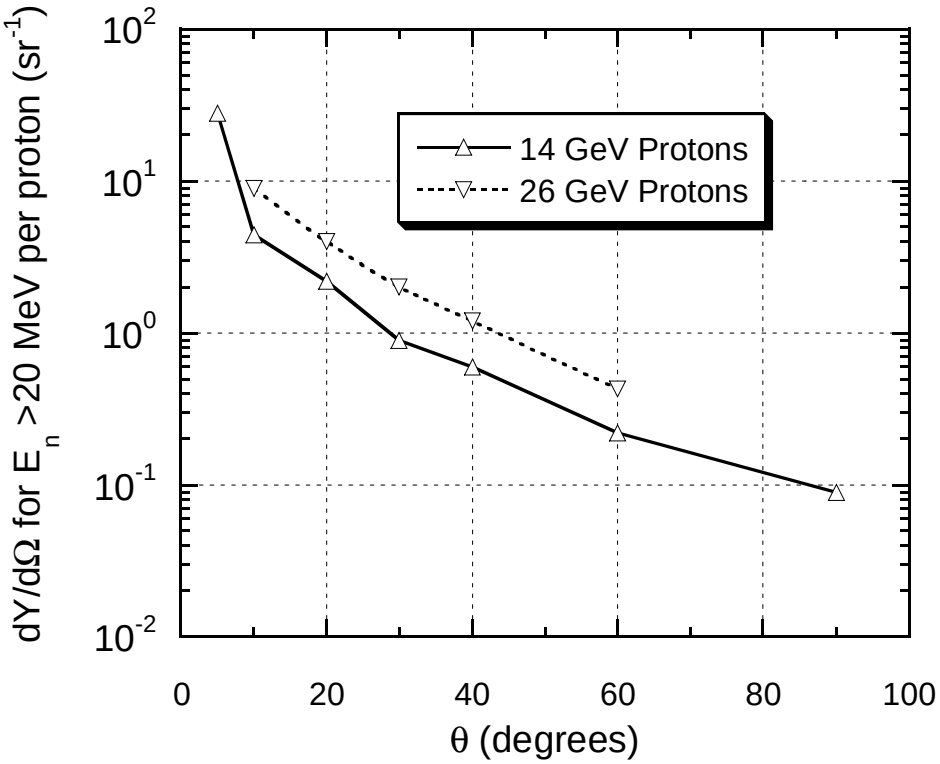

Fig. 4.5 Measurements of the angular distribution, *dY/dΩ,* of neutrons above 20 MeV produced by 14 and 26 GeV protons on a thin beryllium target. The yield is per interacting proton. The lines are drawn to guide the eye. [Adapted from (Gi68).]

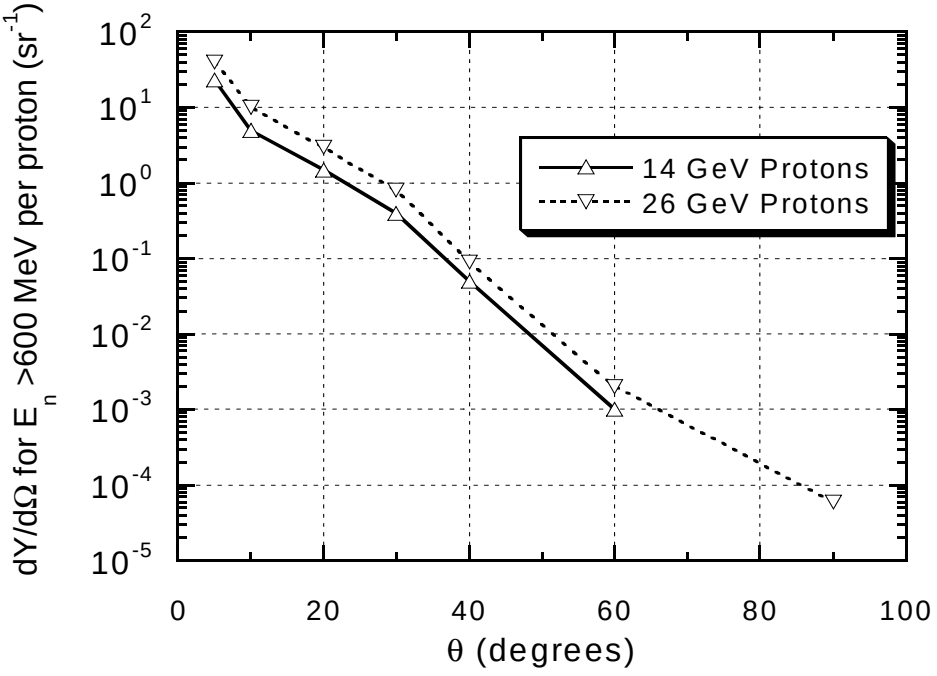

Fig. 4.6 The angular distribution, *dY/dΩ,* of neutrons above 600 MeV produced by 14 and 26 GeV protons on a thin beryllium target. The yield is per interacting proton. The lines are drawn to guide the eye [Adapted from (Gi68).]

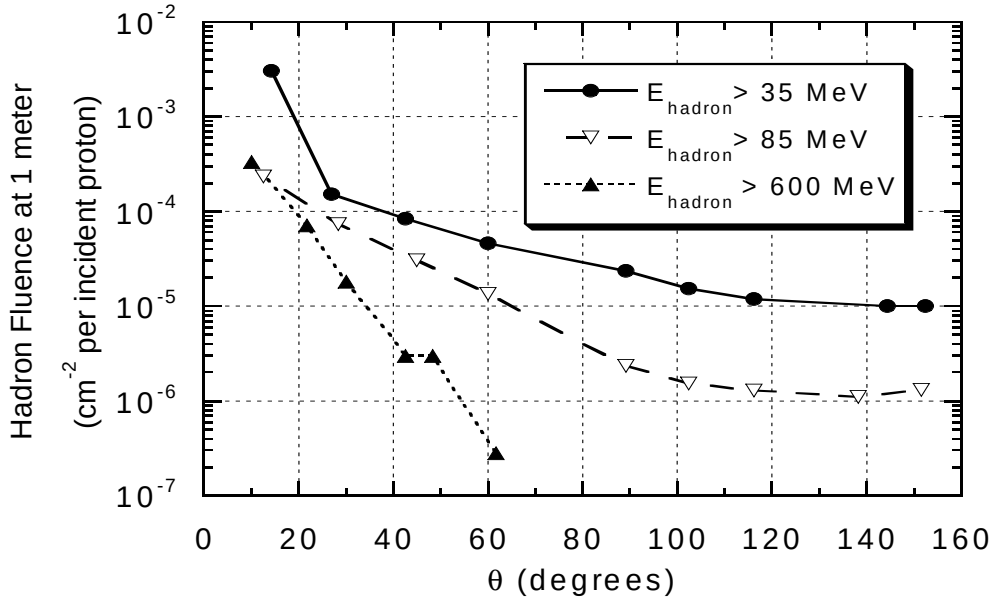

Fig. 4.7 Measured angular distributions of hadron fluence (particles cm^{-2}) at 1 meter from a copper target bombarded by 22 GeV protons. Several choices of hadron energy thresholds are shown. [Adapted from (Ra72).]

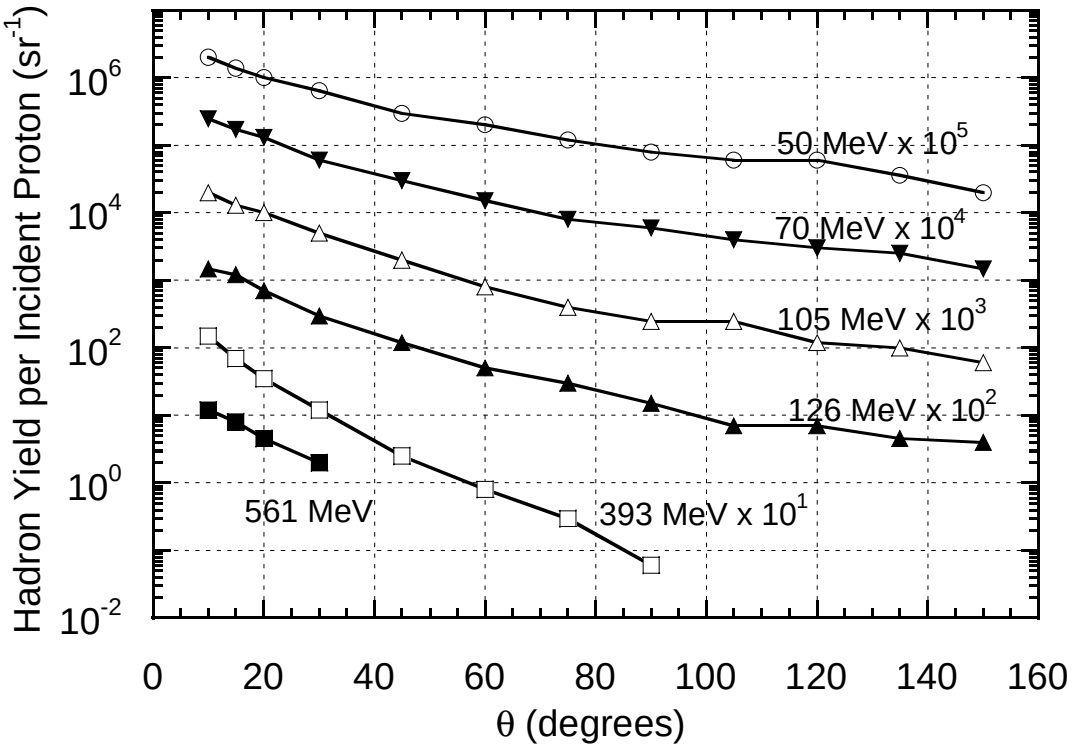

Fig. 4.8 Measurements of hadron yields above different energy thresholds as a function of production angle θ around a 15 cm long copper target bombarded by 225 GeV protons. The data have been multiplied by the indicated factors prior to plotting. The lines are intended to guide the eye. [Adapted from (St85).]

Table 4.1 Summary of removal mean free paths for high energy protons

Material	Density (grams cm^{-3})	Removal Mean Free Path (grams cm^{-2})	Removal Mean Free Path (cm)
hydrogen gas @ STP	9.00×10^{-5}	43.3	4.81×10^{5}
beryllium	1.85	55.5	30.03
carbon	2.27	60.2	26.58
aluminum	2.70	70.6	26.15
iron	7.87	82.8	10.52
copper	8.96	85.6	9.55
lead	11.35	116.2	10.24
uranium	18.95	117.0	6.17
air @ STP	1.29×10^{-3}	62.0	4.81×10^{4}
water	1.00	60.1	60.10
concrete (typical)	2.50	67.4	26.96
silicon dioxide (quartz)	2.64	67.0	25.38
plastics (polyethylene)	0.93	56.9	61.51

Table 4.2 Material-dependent parameters to be used in Eq. 4.3 (from Ra67)

Target	*A*	*B*	*C*
H_2	0.55	-0.30	2.68
Be	0.68	-0.39	3.12
Fe	0.92	-0.75	2.90
Pb	1.14	-1.06	2.73

4.2.3 Sullivan's Formula

For simple radiation protection calculations, Sullivan (Su89) has developed a formula for the fluence, $\Phi(\theta)$, of hadrons with $E_o > 40$ MeV that will be produced at one meter from a copper target struck by protons in the energy region $5 < E_o < 500$ GeV per interacting proton;

$$\Phi(\theta) = \frac{1}{2\left[\theta + \left(35/\sqrt{E_0}\right)\right]^2} \quad (\text{cm}^{-2} \text{ per interacting proton}), \tag{4.4}$$

where E_o is in GeV and θ is in degrees.

This formula also adequately accounts for the distributions of neutrons per incident proton in the region of incident proton energy $0.025 < E_O < 1$ GeV if it is multiplied by, approximately, a factor of two. This equation is plotted in Fig. 4.9, for "lateral" ($\theta \approx 90^o$) and "forward" ($\theta \approx 0^o$) directions.

Of course, the dose equivalent is more directly germane to radiation protection concerns than is the "raw" fluence. In principal, the dose equivalent can be obtained by integrating over the spectrum,

$$H = \int_0^{E_{\max}} P(E)\Phi(E)dE\ , \tag{4.5}$$

or by summation, taking into account the "coarseness" of available data and/or calculations;

$$H = \sum_{j=1}^{m} P_j(E)\Phi_j(E)\Delta_j(E)\ . \tag{4.6}$$

Tesch (Te85) has done this to obtain the dose equivalent at one meter from a copper target ($\theta = 90^o$) bombarded by protons of various energies. The result is plotted in Fig. 4.10. Above about 1 GeV, the dose equivalent is approximately proportional to E_p. Levine (Le72) has measured the angular distribution of absorbed dose for 8 and 24 GeV/c protons incident on a Cu target. The results are in approximate agreement with those found by Tesch.

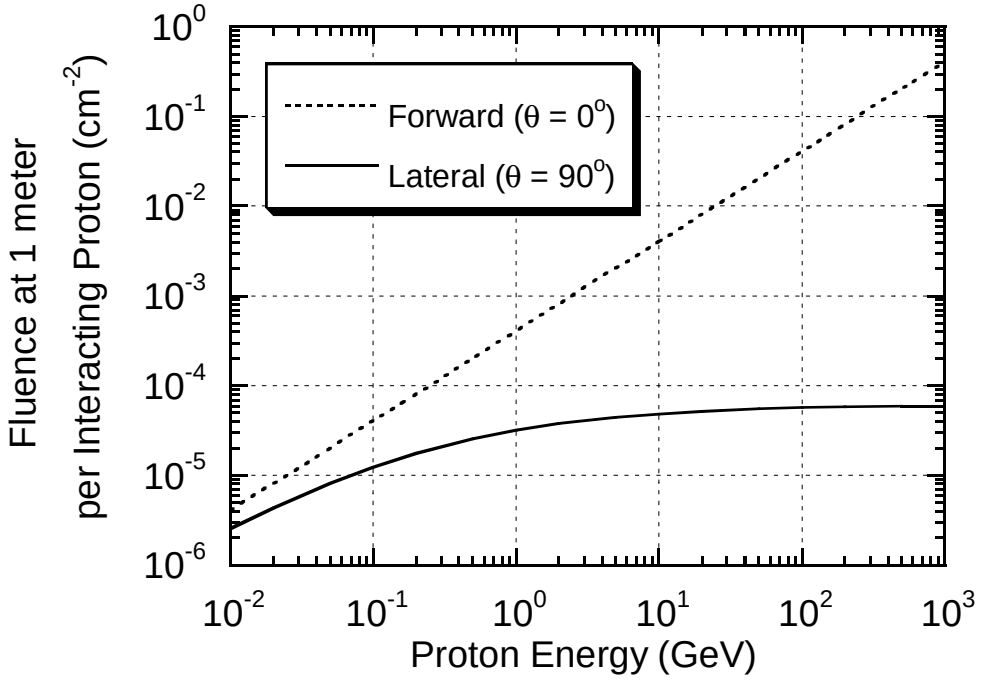

Fig. 4.9 Fluence of hadrons exceeding 40 MeV in energy, per interaction, at 1 meter from the target in both the forward ($\theta = 0^o$) and sideways ($\theta = 90^o$) direction as a function of the interacting proton energy. The proton is interacting in a copper target. [According to (Su89).]

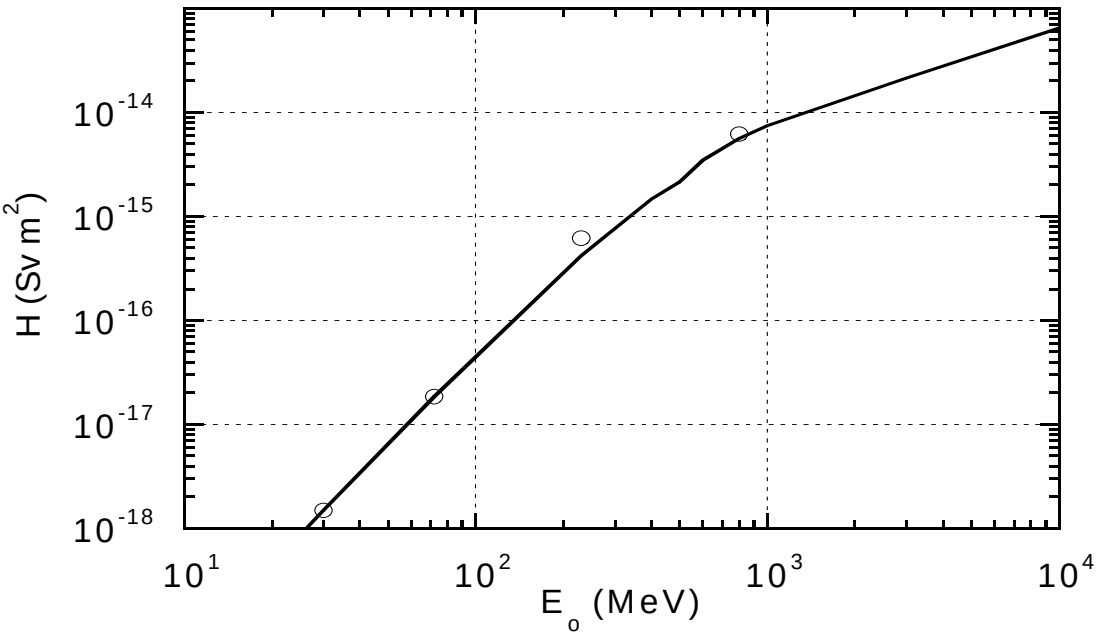

Fig. 4.10 Dose equivalent per proton due to neutrons at $\theta = 90^o$ with energies higher than 8 MeV at a distance of 1 meter from a copper target. The curve is an interpolation between the normalized experimental measurements denoted by the open symbols. [Adapted from (Te85).]

4.2.4 Muons

Muons at proton accelerators arise from two principal mechanisms; from pion and kaon decay and from so-called "direct" production. Production by means of pion and kaon decay proceed as follows where mass of the parent particles, the branching ratio (the percentage of time the parent particle decays by the reaction given), the mean life, τ, and the value of $c\tau$ are also given (PDG96):

$$\pi^{\pm} \rightarrow \mu^{\pm} + \nu_{\mu}; \quad m_{\pi} = 139.6 \text{ MeV}, \quad \tau = 2.60 \times 10^{-8} \text{ s}, \quad (99.99\ \% \text{ branch}),$$
$$c\tau = 7.804 \text{ m, and}$$

$$K^{\pm} \rightarrow \mu^{\pm} + \nu_{\mu}; \quad m_{K} = 493.7 \text{ MeV}, \quad \tau = 1.24 \times 10^{-8} \text{ s}, \quad (63.51\ \% \text{ branch}),$$
$$c\tau = 3.713 \text{ m.}$$

"Direct" muon production, important only at very high energy hadron accelerators, is discussed in more detail in Section 4.7.3.

Muon fields are forward-peaked and, normally, dominated by those from pion decay (except, perhaps at the highest energies). Usually, Monte Carlo techniques are needed to accurately estimate muon intensities. This is because of the need to:

- calculate the production of pions from the proton interactions,
- follow the pions until they decay or interact,
- adequately account for the range-energy relation and range straggling, and
- track the muons to the point of interest, for example, through magnetic fields.

4.3 Primary Radiation Fields at Ion Accelerators

Large portions of Section 4.2 have discussed general considerations that are appropriate the primary radiation fields generated by accelerated ions as well as to protons. In this section, special issues found in radiation fields produced by ions other than protons are described. Because the ionization range for ions of a given kinetic energy decreases as a function of ion mass, targets become effectively "thicker" as the ion mass increases.

4.3.1 Light Ions (Ion Mass Number, $A < 5$)

For such ions there are exothermic reactions that should be treated as special cases. Noteworthy examples (followed by their reaction Q-values, Q_v, in parentheses) are:

$D(d,n)^3He$ (Q_v = 3.266 MeV)
$^9Be(\alpha,n)^{12}C$ (Q_v = 5.708 MeV)
$^3H(d,n)^4He$ (Q_v = 17.586 MeV).

In some cases monoenergetic beams of neutrons can be produced using these or the following slightly endothermic reactions:

$^{12}C(d,n)^{13}N$ (Q_v = -0.281 MeV)
$T(p,n)^3He$ (Q_v = -0.764 MeV)
$^7Li(p,n)^7Be$ (Q_v = -1.646 MeV).

The energies of such neutrons can range from 0 to 24 MeV for bombarding energies up to 10 MeV.

In general, deuteron stripping and breakup reactions, (d,n), have the highest yields because the binding energy of the deuteron is only 2.225 MeV. In effect, one gets an extra neutron "for free". Furthermore, the neutrons due to deuteron stripping reactions typically have a kinetic energy of about half that of the incident deuteron if the latter has a kinetic energy that is large compared with the binding energy of the target nucleus. This phenomenon is especially pronounced at the lower energies. In the low energy region, and especially with light ions, one should carefully consider all possible reactions given the materials present in conjunction with the ions that are being accelerated. Patterson and Thomas (Pa73) have summarized total neutron yields for light ions. In general, the yields for the various light ions behave similarly to those due to protons. That is, the yield is within, typically, a factor of three of that expected for proton beams. A good measurement of neutron yields due to 40 MeV α-particles has been provided by Shin et al. (Sh95). Higher energy neutron production data for 640 and 710 MeV α-particles has been provided by Cecil et al. (Ce80).

4.3.2 Heavy Ions (Ions with $A > 4$)

At higher energies and especially at higher masses, neutron yield and dose equivalent data and calculations are very sparse. The data is usually normalized in terms of kinetic energy per atomic mass unit, the **specific energy**, expressed in units of MeV/amu, or kinetic energy per nucleon because reaction parameters generally scale to that parameter. In the literature the technical distinction between energy/amu and energy/nucleon is often ignored. In the range up to 20 MeV/amu, Ohnesorge et al. (Oh80) have measured dose equivalent rates at one meter at $\theta = 90^o$ from thick targets of iron, nickel, or copper

bombarded by ^{4}He, ^{12}C, ^{14}N, ^{16}O, and ^{20}Ne beams. The dose equivalent was found to be essentially independent of ion type as a function of specific energy. At 10 MeV/amu, a value of 6.3 x 10^{-18} Sv/incident ion was measured while at 20 MeV/amu, a value of 3.6 x 10^{-17} Sv/incident ion was found. Other data relevant to this general energy region are exemplified by those of Hubbard et al. (Hu60), Aleinikov et al (Al85), and especially Nakamura (Na85).

Tuyn et al. (Tu84) reports studies done with 86 MeV/amu ^{12}C ions incident on Fe targets slightly thicker than interaction length. The measurements are shown in Fig. 4.11. At a specific energy of 155 MeV/amu, Britvitch et al. (Br99) have measured energy spectra and total neutron yields and angular distributions for ^{4}He, ^{12}C, and ^{16}O ions stopping in a thick target of an alloy of tungsten, nickel, and copper commonly known as "Hevimet". The differential yields, $dY/d\Omega$, were fit by the form,

$$\frac{dY}{d\Omega} = C\exp(-\beta\theta), \tag{4.7}$$

with the total yields being found by the integration,

$$Y_{total} = 2\pi\int_0^{\pi} d\theta \sin\theta \frac{dY(\theta)}{d\Omega} = 2\pi C \frac{\left[\exp(-\beta\theta)+1\right]}{(\beta^2+1)}. \tag{4.8}$$

The results are presented in Fig. 4.12. The total neutron yield for ^{4}He, ^{12}C, and ^{16}O was found to be 4.90, 1.56, and 1.74 neutrons per incident ion, respectively.

Clapier and Zaidins (Cl83) have surveyed a sample of data from 3 to 86 MeV/amu and have been able to fit the fluence angular distribution follows the following functional form:

$$\Phi(\theta,\xi) \approx \frac{1}{4\pi}\left[\frac{1}{\ln\{1+1/\xi\}}\right]\left[\frac{1}{\xi+\sin^2(\theta/2)}\right], \tag{4.9}$$

where θ is in degrees and the fitting parameter ξ is determined by

$$\xi = \frac{\Phi(90^O)}{\Phi(0^O)-\Phi(90^O)} = \frac{1}{\Phi(0^O)/\Phi(90^O)-1}\ , \tag{4.10}$$

where $\Phi(\theta,\xi)$ is the fluence or dose equivalent at θ. These same authors have found that the total yield, Y (neutrons/ion) can be approximately fit as a function of the projectile atomic number, Z, and the specific energy, W (MeV/amu). They found

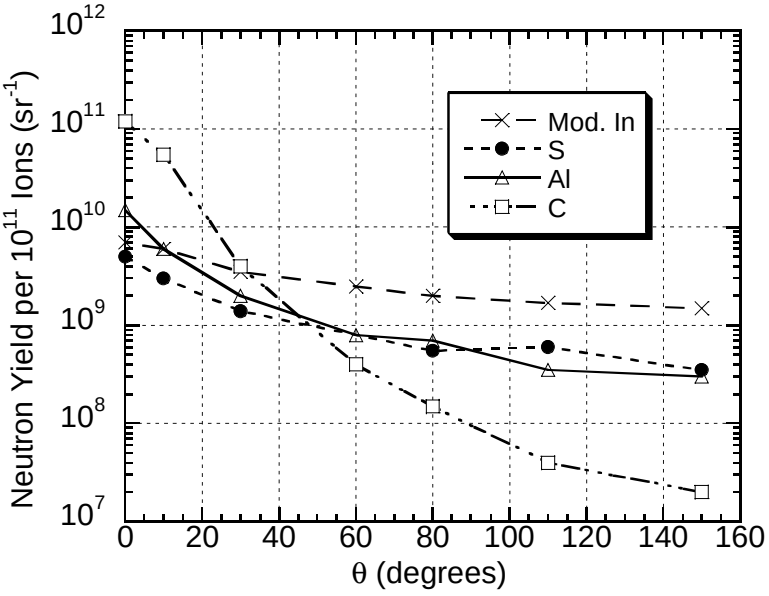

Fig. 4.11 Measured neutron yields per 10^{11} incident ions at 86 MeV/amu ^{12}C ions incident on an iron target. Activation detectors with the following sensitive regions in neutron energy, E_n, were used: moderated indium foils ($0.4 < E_n < 107$ eV), ^{33}S(n, p)^{32}P ($E_n > 3$ MeV), ^{27}Al(n, α)^{24}Na ($E_n > 7$ MeV), and ^{12}C(n,2n)^{11}C ($E_n > 20$ MeV). The lines are intended to guide the eye. [Adapted from (Tu84).]

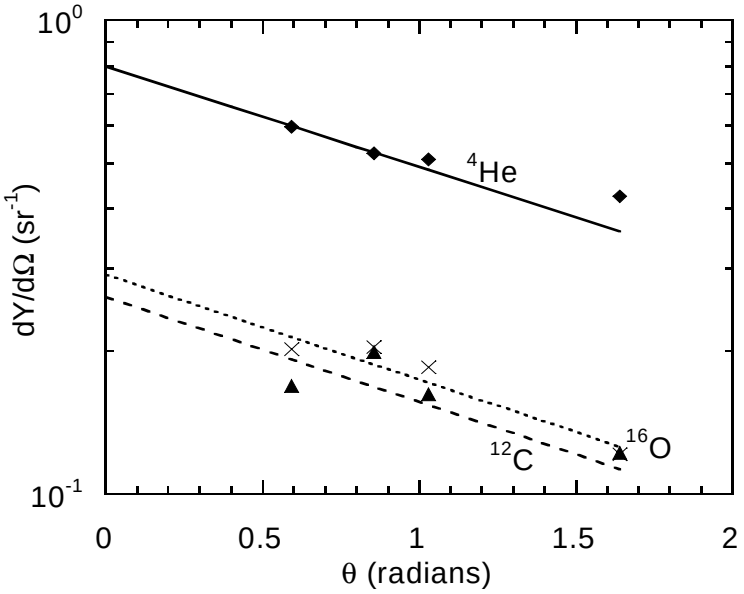

Fig. 4.12 Neutron yields per incident ion for 155 MeV/amu ions reported by Britvich et al. (Br99). The diamonds are measurements for ^{4}He which were fitted by parameters (C{neutrons/incident ion) and β{sr^{-1}} of (0.8, 0.49) as defined by Eqs. (4.7) and (4.8). The results for ^{12}C are denoted by triangles and were fit by (C,β) values of (0.26, 0.51). The results for ^{16}O are denoted by crosses and were fit by (C,β) values of (0.29, 0.51).

essentially no dependence on atomic number of the target. The expressions that result are:

$$Y = (W, Z) = C(Z)W^{\eta(Z)} \qquad \text{with} \tag{4.11}$$

$$\eta(Z) = 1.22\sqrt{Z} \qquad \text{and} \tag{4.12}$$

$$C(Z) = \frac{1.96\times10^{-4}}{Z^{2.75}} \exp\left\{-0.475\left(\ln Z\right)^2\right\} \tag{4.13}$$

These authors have identified values of the parameters *C(Z)* and $\eta(Z)$ that are presented in Table 4.3. They also give a few examples of the parameter, ξ, in the expression for fitting the angular distribution. Values of 0.07 for uranium incident on uranium at 9 MeV/amu, 0.025 for neutrons of energy E_n < 20 MeV produced by 86 MeV/amu ^{12}C incident on iron, and 3 x 10^{-4} for neutrons of energy E_n > 20 MeV produced by 86 MeV/amu ^{12}C incident on iron are reported. The latter result is based on an analysis of the data presented in Fig. 4.11. One, in principle, could use values given in Table 4.3 or the direct calculation using Eqs. (4.12) and (4.13) and obtain some idea of the uncertainties inherent in this fit of such a broad range of data. However, the uncertainties in this type of fit are quite large due to the functional forms that were used.

Table 4.3 Values of the parameters $\eta(Z)$ and $C(Z)$ as expressed in Eq (4.11-4.13). [Adapted from (Cl83).]

Atomic Number	Element	$\eta(Z)$	$C(Z)$
1	hydrogen	1.5	1.7 x 10^{-4}
2	helium	2.6	3.9 x 10^{-6}
6	carbon	1.7	2.5 x 10^{-6}
8	oxygen	3.6	3.6 x 10^{-7}
10	neon	7.0	2.7 x 10^{-10}
18	argon	7.0	5.1 x 10^{-11}
36	krypton	7.9	6.0 x 10^{-12}
82	lead	11.0	1.7 x 10^{-13}

McCaslin, et al. (McC85) measured the angular distribution of yields of 670 MeV/amu Ne and Si ions stopped in a copper target. For 670 MeV/amu ^{20}Ne ions including all neutrons above 6.5 MeV at a radius of 1 meter, McCaslin found:

$$\Phi(\theta) = 372\frac{1}{\theta} \text{ neutrons m}^{-2} \text{ per ion for } 2^o < \theta < 180^o, \ \theta \text{ in degrees.} \tag{4.14}$$

For incident 670 MeV/amu ^{20}Ne ions including all neutrons above 20 MeV;

$$\Phi(\theta) = 248e^{-0.2\theta} \text{ neutrons m}^{-2} \text{ per ion for } 0^o < \theta < 20^o, \ \theta \text{ in degrees, and} \qquad (4.15)$$

$$\Phi(\theta) = 10e^{-0.038\theta} \text{ neutrons m}^{-2} \text{ per ion for } 20^o < \theta < 120^o, \ \theta \text{ in degrees.} \qquad (4.16)$$

The neutron yields at this high specific energy for heavy ions turn out to be quite large. By integrating the above over all angles, one finds a total yield of 73.9 neutrons/incident ion for $E_n > 6.5$ MeV for ^{20}Ne incident ions. Fig. 4.13 is comparison of total neutron yields for representative heavy ions with the yields found for protons as a function of specific energy.

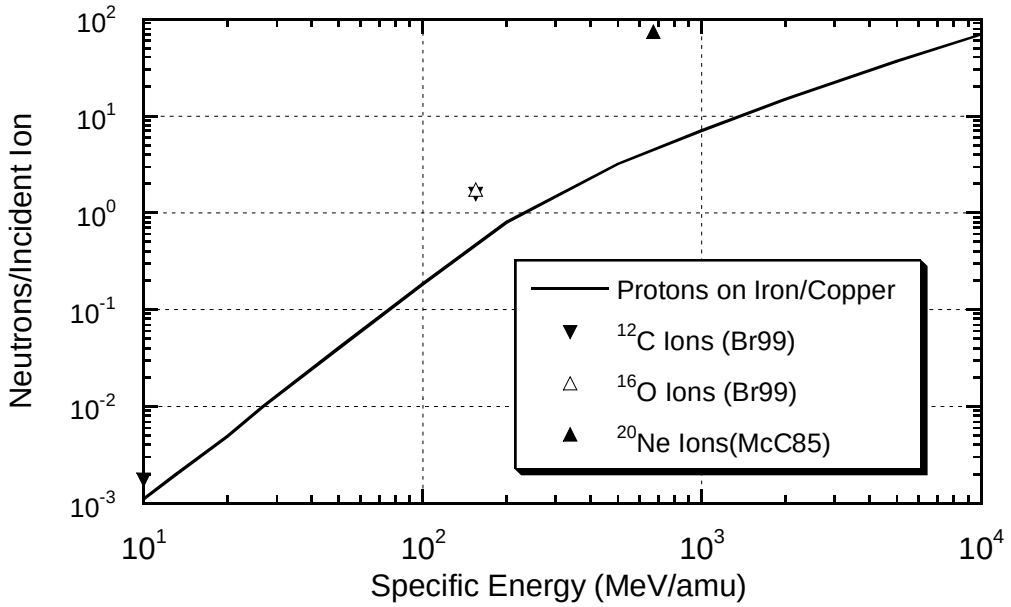

Fig. 4.13 Neutron yields as a function of specific energy for selected heavy ion projectiles as reported by the cited references. The curve for protons is that of Fig. 4.1 for protons incident on iron or copper targets. The data points for ^{12}C and ^{16}O are for a Hevimet target while the datum for ^{20}Ne is for a copper target.

4.4 Hadron (Neutron) Shielding for Low Energy Incident Protons (E_o < 15 MeV)

This region is especially complex because it is the region of significant nuclear structure effects. There are many resonances associated with compound nucleus that can be excited and there also many nuclear reaction channels leading to a large number of nuclear excited states up to 20 MeV in excitation energy which have a wide variety of nuclear structure quantum numbers and very narrow widths in energy.

The method most commonly used to calculate shielding thicknesses is that of **removal cross section theory**.

According to Clark (Cl71) there are three principles involved here:

- "The shield must be sufficiently thick and the neutrons so distributed in energy that only a narrow band of the most penetrating source neutrons give any appreciable ultimate contribution to the dose outside the shield."

- "There must be sufficient hydrogen in the shield, intimately mixed or in the final shield region, to assure a very short characteristic transport length from about one MeV to absorption at or near thermal energy."

- "The source energy distribution and shield material (non-hydrogeneous) properties must be such as to assure a short transport distance for slowing down from the most penetrating energies to 1 MeV."

It has been found that the transmission of dose equivalent, H, as a function of shield thickness, t, is approximately given for these neutrons by

$$H(t) = \Phi_0 PG \exp(-\Sigma_r t), \tag{4.17}$$

where Φ_0 is the fluence before the shielding (calculated from neutron yield information), P is the dose equivalent per fluence conversion factor (obtained by performing any needed integration over the energy spectrum), G is a "geometry factor", t (cm) is the

thickness of the shield. For parallel beams, $G = 1$ while for an isotropic point source, $G = 1/r^2$. Σ_r is the **macroscopic removal cross section**:

$$\Sigma_r = \frac{0.602\sigma_r\rho}{A} \quad (\text{cm}^{-1}), \tag{4.18}$$

where σ_r is the **microscopic removal cross section** in barns, ρ is the density (g cm^{-3}) and A is the mass number. For mixtures of n materials,

$$\Sigma_r = \sum_{i=1}^{n}\left(\frac{\Sigma_{ri}}{\rho}\right)_i \rho_i \tag{4.19}$$

where the quantity in parentheses is the **removal cross section per unit mass** of the i^{th} constituent and ρ_i is the **partial density** of the i^{th} material. In this formulation the overall density is equal to the sum of the partial densities.

For $A > 8$,

$$\sigma_r \approx 0.21\, A^{-0.58} \quad \text{(barns)} \tag{4.20}$$

for neutrons of approximately 8 MeV. Figure 4.14 taken from (Pa73) shows the values of σ_r as a function of mass number at this energy. Table 4.4 gives representative values for σ_r for some energies where this approach is applicable.

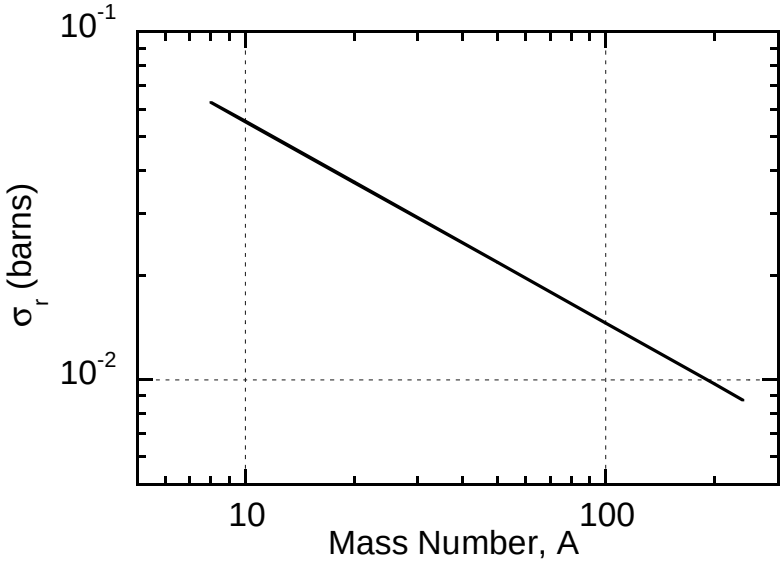

Fig. 4.14 Removal cross sections per unit atomic mass for fission neutrons as a function of mass number at a neutron energy of 8 MeV. Over the range $8 \leq A \leq 240$, the values are well fit by Eq. (4.20). [Adapted from (Pa73)].

Table 4.4 Removal cross-section data, σ_r (barns) for low energy neutrons. The typical accuracy is quoted to be ± 5 %. [Adapted from (Pa73).]

Element	1 MeV	Fission Spectrum	2.9 MeV	4 MeV	6.7 MeV	14.9 MeV
Carbon		0.9	1.58	1.05	0.83	0.50
Aluminum		1.31				
Iron	1.1	1.96	1.94	1.98	2.26	1.60
Copper		2.04				
Lead		3.28	2.70	3.44	3.77	2.95

The use of removal cross sections describe attenuation data rather effectively despite the fact that as more shielding is penetrated, neutrons of lower energy tend to dominate the spectrum over those found in the few MeV region.

4.5 Limiting Attenuation at High Energy

The most important feature of neutron shielding at higher energy accelerators is the fact that the attenuation length becomes an approximate constant at high energy. As the energy increases, the neutron inelastic cross sections also increase rapidly until about 25 MeV where they level off and then fall rapidly with energy in the region $25 < E_n < 100$ MeV to a value which becomes independent of energy. Lindenbaum was the first to make this observation (Li61). The result is that high energy neutron beams attenuate approximately exponentially with an attenuation length, λ_{atten}, that is rather insensitive to energy. Thus, in units of length,

$$\lambda_{atten} = \frac{1}{N\sigma_{in}} \quad \text{(cm)}, \tag{4.21}$$

where σ_{in} is the inelastic cross section, roughly equivalent to the so-called "absorption cross section" and N is the number of absorber nuclei per unit volume. This cross section specifically does not include elastic scattering and so is always smaller than the total cross section. In a simple-minded approach, this cross section can be taken to be approximately geometric and the nucleon radius is taken to be 1.2×10^{-13} cm. It then follows (see Problem 5) that in the high energy limit, one might multiply by the density to get

$$\rho\lambda_{atten} = 36.7A^{1/3} \qquad \text{(g cm}^{-2}\text{)}. \tag{4.22}$$

Fig. 4.15 illustrates the neutron inelastic cross sections for several materials up to a kinetic energy of 1.4 GeV beyond which the value is essentially constant. These results were verified by historic cosmic ray data and are well-represented by

$$\sigma_{in} = 43A^{0.69} \qquad \text{(mb)}. \tag{4.23}$$

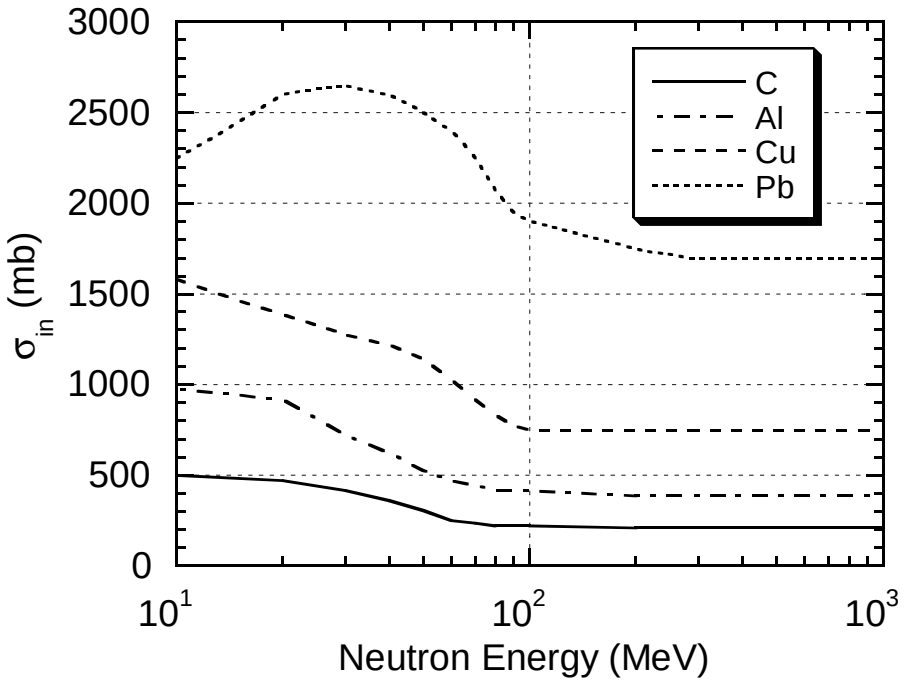

Fig. 4.15 Inelastic neutron cross sections as a function of energy in the range 1 to 1000 MeV. [Adapted from (Li61).]

In the high energy limit, the **interaction length**, λ_{inel} , is thus given by:

$$\lambda_{inel} = \frac{\rho}{N\sigma_{in}} = 38.5A^{0.31} \text{ (g cm}^{-2}\text{)}. \tag{4.24}$$

This **geometric approximation** is thus reasonably accurate. Values of the high energy interaction lengths are available for many different materials and representative examples are found in Table 1.2. Figure 4.16 shows the results for absorption cross sections based upon these values. Schopper et al. (Sc90) has provided extensive tabulations of the value of σ_{in} (mb) for a variety of particles, energies, and materials in the high energy region as functions of particle momenta up to 10 TeV/c.

The saturation of attenuation length for concrete as a function of particle energy is especially important, due to the widespread utilization of this material for hadron shielding. Figure 4.17 gives the results for both neutrons and protons. An important feature of these results is the equivalence of the attenuation lengths for protons and neutrons at high energies. Due to the similarities of chemical composition, results for soil shielding in this energy regime can be taken to be the same when λ is expressed in units of areal density, e.g., g cm^{-2}.

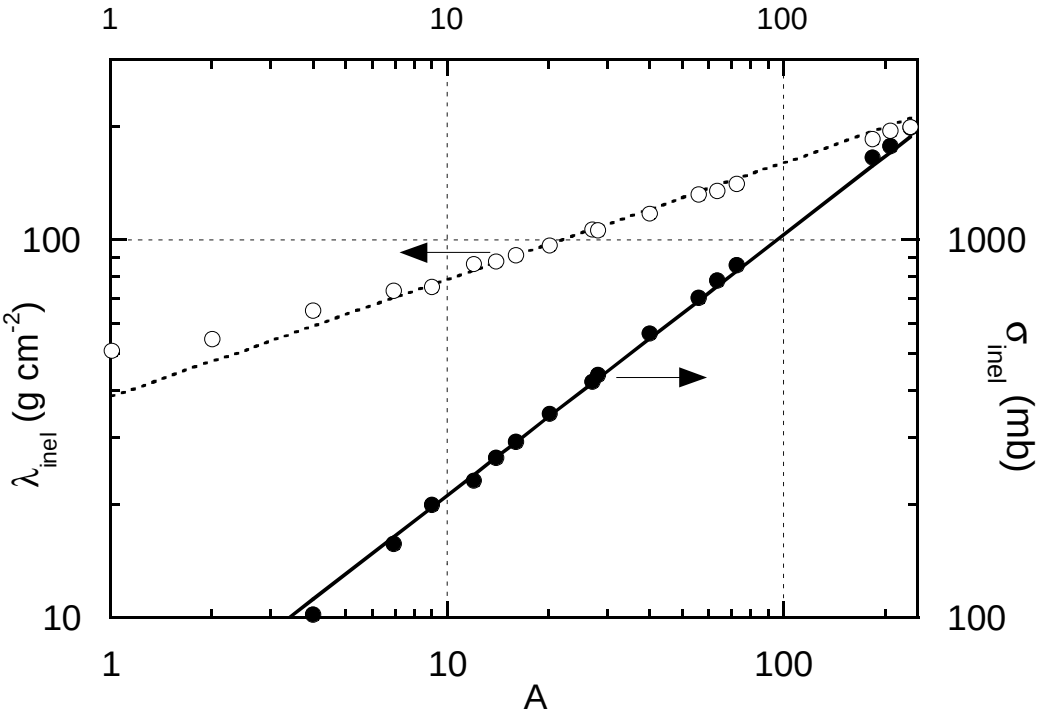

Fig. 4.16 Inelastic mean free path and cross section as a function of mass number, *A*. [Adapted from (Pa73).]

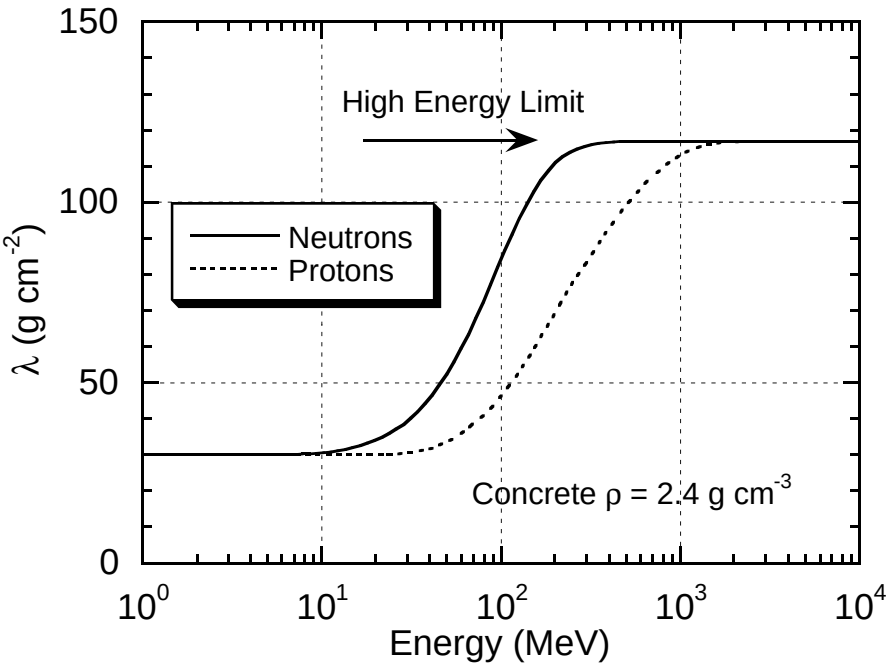

Fig. 4.17 The variation of the attenuation length λ for monoenergetic neutrons and protons in concrete shielding as a function of neutron energy. The high energy limit is 117 g cm^{-2}. [Adapted from (Th88).]

4.6 Intermediate and High Energy Shielding-The Hadronic Cascade

4.6.1 The Hadronic Cascade from a Conceptual Standpoint

The **hadronic cascade** is initiated at proton accelerators when the beam interacts with components to produce neutrons and other particles. Such cascades can also arise at electron accelerators since, as described in Chapter 3, high energy secondary hadrons can also result from electromagnetic interactions.

The collision of a high energy nucleon with a nucleus produces a large number of particles; pions, kaons, and other nucleons as well as fragments of the struck nucleus. According to Thomas and Stevenson, above 1 GeV and at forward angles, the pions, protons, and neutrons, can be nearly equal in number (Th88). The neutrons may be classified as either **evaporation neutrons** or **cascade neutrons**, as discussed in Section 4.2.2.2. To review, evaporation neutrons originate as decays from excited states of residual nuclei and average a few MeV in energy. These neutrons tend to be isotropically distributed. Cascade neutrons are emitted by direct impact and their spectrum extends in energy up to the incident energy with diminishing probability following a spectrum roughly characterized as having an energy dependence proportional to *1/E*.

As the proton kinetic energy increases, other particles, notably $\pi^{\pm}$ and $K^{\pm}$, play roles in the cascade when their production becomes energetically possible. They are absorbed with absorption lengths comparable in magnitude to, but not identical with those of protons. These particles also decay into muons. Because of their long ionization ranges and lack of nuclear interactions, muons provide a pathway for energy to escape the cascade.

Hadrons, principally nucleons, with $E_o > 150$ MeV propagate the cascade. This is clear from the attenuation lengths shown in Fig. 4.15. Nucleons in the range $20 < E_n < 150$ MeV also transfer their energy predominantly by nuclear interactions but their energy gets distributed over many particles of all types energetically possible. The charged particles produced in such cascades are generally ranged-out in material or create yet other particles in the cascade. The role played by the energy of approximately 150 MeV for hadronic cascades is qualitatively somewhat analogous to that of the critical energy for electromagnetic cascades.

Neutral pions (π^o) are produced when the kinetic energy of the incident proton significantly exceeds the π^o rest energy of 135.0 MeV. The π^o mean life, $\tau = (8.4 \pm 0.6) \times 10^{-17}$s is very short so that for the π^o, $c\tau = 25.1$ nm. Hence, π^o's do not travel very far at all before decaying. The principal decay (99 % branching ratio) is into two γ-rays. An energetic π^o thus appears as two forward-peaked photons each with half of the π^o's total energy. The decay photons from π^o decay readily initiate electromagnetic cascades along with the hadronic one. It is possible for the electromagnetic channel to feed back into the hadronic cascade because it, too,

produces high energy hadrons. However this effect is generally of little importance and, for most shielding calculations, the electromagnetic component of a hadronic cascade can be ignored. The exceptions principally involve energy deposition calculations at forward angles (small values of θ). In fact, at hundreds of GeV, electromagnetic cascades dominate the energy deposition at very forward angles (i.e., at very small values of θ). This feature can have important ramifications if one needs to consider radiation damage to equipment and, as an example, the heat load on cryogenic systems.

In general, the neutrons are the principal drivers of the cascade because of the ionization energy loss for pions and for protons below 450 MeV where the ionization range becomes roughly equal to the interaction length. Also, any magnetic fields that are present which can deflect and disperse charged particles present will not, of course, affect the neutrons. Furthermore, neutrons can be produced at large values of θ compared with the forward-peaked pions. These phenomena, in general, apply also to ions heavier than the proton with suitable corrections (especially at low energies) for nuclear structure effects. Scaling of proton results for heavier ions will, in general, roughly be according to the specific energy (MeV/amu). Figure 4.18 due to Torres (To96) is a schematic flow chart of the hadronic cascade process.

4.6.2 A Simple One-Dimensional Cascade Model

A simple, one-dimensional model of the hadronic cascade was first proposed by Lindenbaum (Li61). This approach gives some "intuition" into the nature of the hadronic cascade. Figure 4.19 defines the geometry. Suppose one initially has N_o incident high energy nucleons. After an individual collision, one of them continues in its original direction at a reduced energy but with the same attenuation length, λ, or will generate one or more secondary particles also with the same λ. The value of λ is approximately constant due to the limiting attenuation at high energy. This process continues until a number of collisions, *n*, have occurred which are sufficient to degrade the particle energies to approximately 150 MeV, below which energy the inelastic cross sections greatly increase (see Fig. 4.15). At this point a given particle is said to be removed from the cascade. For the present discussion, it is assumed that *n* is an integer when, in reality, it has a statistical distribution. Thus, referring to the Fig. 4.19, the number ν_1 that reach $x = z$ having made no collisions is

$$\nu_1 = N_0 \exp(-z / \lambda) . \tag{4.25}$$

Suppose that there is one collision between 0 and *z*. The number, ν_2, that reach *z* is given by the product of the number that reach elemental coordinate *dr* and the probability of subsequently reaching *z*, times the probability of interacting in *dr*, dr/λ, times the **multiplicity**, m_1, of particles produced in the first interaction. Integrating over *dr*:

$$\int_0^z \left[N_0 \exp\{-r / \lambda\} \right] \left[\exp\{-(z-r) / \lambda\} \right] \left[m_1 \frac{dr}{\lambda} \right] = \left(N_0 m_1 \frac{z}{\lambda} \right) \exp(-z / \lambda) = \nu_2 . \tag{4.26}$$

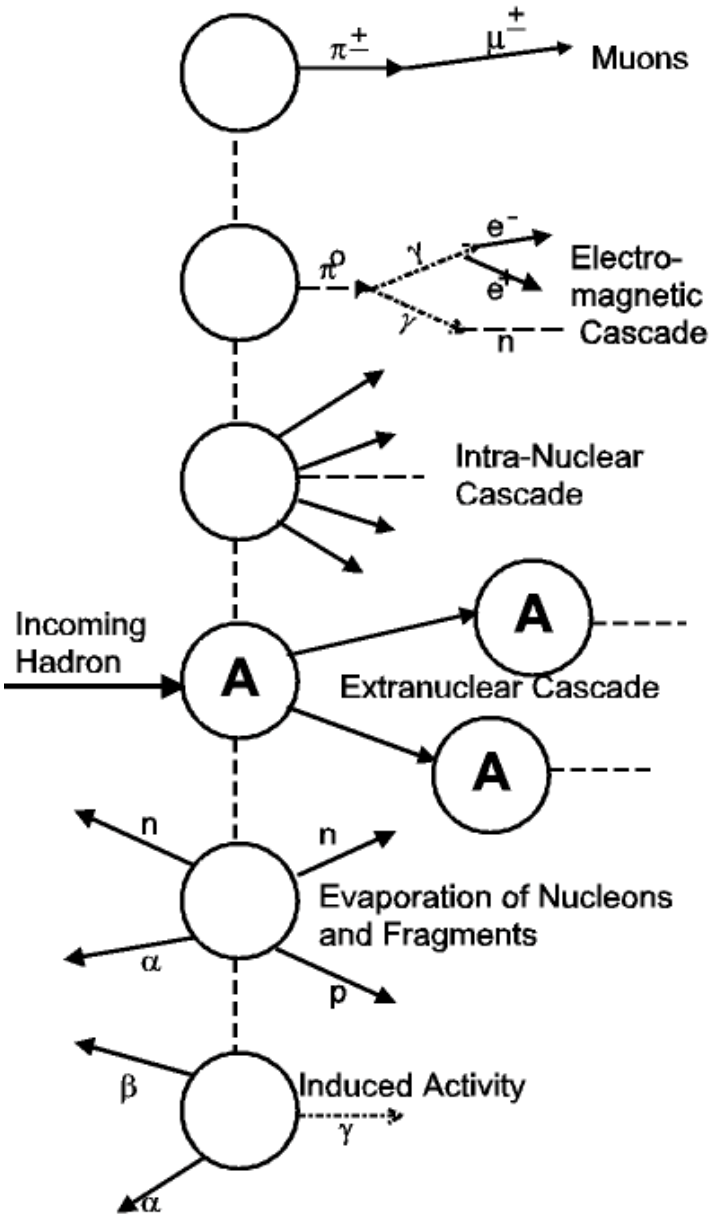

	Most Numerous Participants	Time Scale (seconds)	Typical Energy per Particle (MeV)	Per Cent of Energy Deposition
Muons	$\pi, K \rightarrow \mu$	10^{-8}	any	10
Electro-magnetic Cascade	$\pi^0 \rightarrow e,\gamma$	10^{-16}	any	20
Intra-Nuclear Cascade	p, n, π, K	10^{-22}	<200	30
Extranuclear Cascade	p, n, π, K	10^{-23}	>200	30
Evaporation of Nucleons and Fragments	p, n, d, α	10^{-19}	<30	10
Induced Activity	α, β, γ	seconds to years	<10	<1

Fig. 4.18 Schematic representation of the development of the hadronic cascade and the major participants in any given path. The approximate time scales, the typical energies, and the fraction of energy deposition due to these participants are also shown. [Adapted from (To96).]

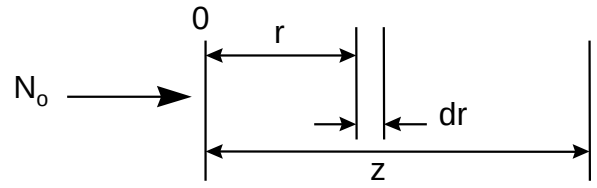

a)

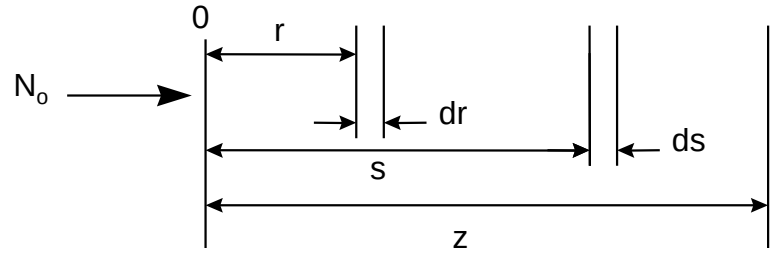

b)

Fig. 4.19 a) Single collision geometry for the Lindenbaum approximation. b) Two collision geometry for the Lindenbaum one-dimensional model. [Adapted from (Th88).]

Now suppose there two collisions occur. The number, ν_3, that reach z is the product of those that reach s having made one collision, multiplied by the probability of subsequently reaching z, times the multiplicity in the second interaction m_2, times the probability of interacting in ds;

$$\int_0^z \left[N_0 m_1 \frac{s}{\lambda} \exp\{-s/\lambda\} \right] \left[\exp\{-(z-s)/\lambda\} \right] \left[m_2 \frac{ds}{\lambda} \right] =$$

$$\left(N_0 m_1 m_2 \frac{z}{\lambda^2} \right) \exp(-z/\lambda) \int_0^z s\,ds = \left(N_0 m_1 m_2 \frac{z^2}{2\lambda^2} \right) \exp(-z/\lambda) = \nu_3 \qquad (4.27)$$

Therefore, with n defined as above, one can write:

$$N_n(x) = N_0 \beta_n(z/\lambda) \exp(-z/\lambda)\,, \qquad (4.28)$$

where β is a "buildup" factor,

for $n = 1$ $\quad N_1 = \nu_1 \quad \beta_1 = 1$,

for $n = 2$ $\quad N_2 = \nu_1 + \nu_2 \quad \beta_2 = 1 + (m_1 z/\lambda)$, and

for $n = 3$ $\quad N_2 = \nu_1 + \nu_2 + \nu_3 \quad \beta_3 = 1 + (m_1 z/\lambda) + (m_1 m_2 z^2/2\lambda^2)$.

For arbitrary *n*,
$$\beta_n = 1 + \frac{m_1 z}{\lambda} + \frac{m_1 m_2 z^2}{2\lambda^2} + \ldots + \frac{1}{n!}\left(\frac{z^n}{\lambda^n}\right)\prod_{i=1}^{n} m_i \qquad (4.29)$$

Thus, this buildup factor is a monotonically increasing function of *z*. If $m_1 = m_2 = \ldots = m$ (i.e., assuming that the multiplicity stays the same for all interactions in this simple model) and *n* is large, comparison with the series expansion of the exponential function reveals that β_n approximates an exponential dependence on *z*. The condition on *n* implies that the shield must be quite thick. The general result is that the attenuation length of the cascade, λ_{cas}, is somewhat larger than the value of the interaction length, λ, for a single interaction. Figure 4.20 is a plot of the number of particles after three generations as a function of x/λ ($m = 2$ and $n = 3$). The exponential region is not completely achieved until $z/\lambda \approx 10$. In concrete, this represents a depth of approximately 1200 g cm^{-2}. Figure 4.20 compares this estimate with data from an experimental measurement of Citron, et al. (Ci65) obtained in an experiment with 19.2 GeV/c protons incident on an iron slab which approximated the conditions on *m* and *n* mentioned above. Analytical approaches such as this one are constructive qualitatively but have severe limitations, among which are:

- the restriction to one dimension,
- the neglect of ionization energy losses and escape of energy carried by muons,
- the neglect of elastic and multiple Coulomb scattering,
- the assumption that <u>all</u> secondary particles go forward,
- the assumption that multiplicities are <u>not</u> dependent on energy and particle type,
- the assumption that λ is a constant for all particles at all energies, and
- the neglect of radiative and electromagnetic cascade effects.

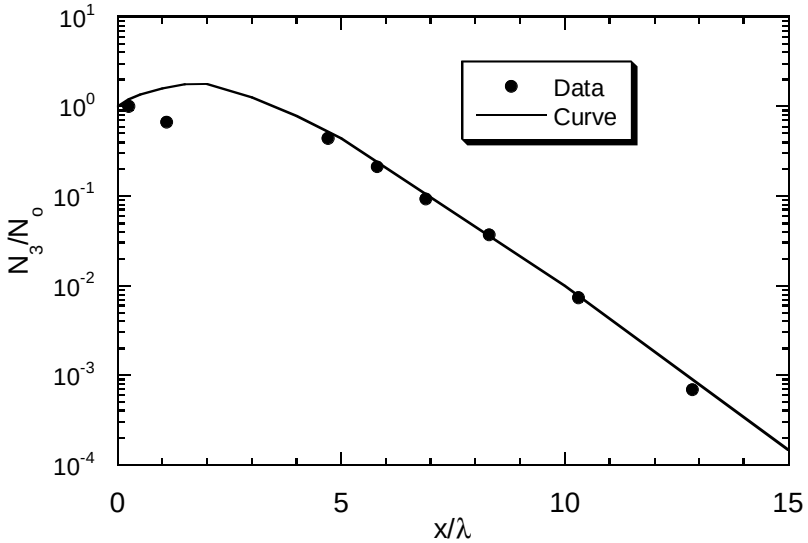

Fig. 4.20 Development of a one-dimensional cascade in the Lindenbaum approximation with $n = 3$ and $m = 2$ from Thomas and Stevenson (Th88) which is labeled "curve" compared with the laterally integrated star density in nuclear emulsions produced by a 19.2 GeV/c proton beam incident on an iron slab measured by Citron et al. (Ci65) which is labeled "data".

4.6.3 Semiempirical method, the Moyer Model for a Point Source

A number of references (Pa73, IC78, Sc90, Ro76, St82, Th84, McC87, Te83, Te85, McC85, Co82a, and Co85a) bear on the development of this model that is based, predominantly, on an exponential approximation with constants fitted to actual data spanning the range of proton beam energies from 7.4 to 800 GeV. The summary of this method here is largely taken from Patterson and Thomas (Pa73) and Schopper et al. (Sc90). This so-called **Moyer Model** was first developed by B. J. Moyer to solve particular shielding problems related to the Bevatron at the Lawrence Radiation Laboratory. The model predates the development of large, fast computers and advanced Monte Carlo techniques but is still useful as means of checking more sophisticated calculations.

This model will be discussed for the situation shown in Fig. 4.21 for a "point" target source.

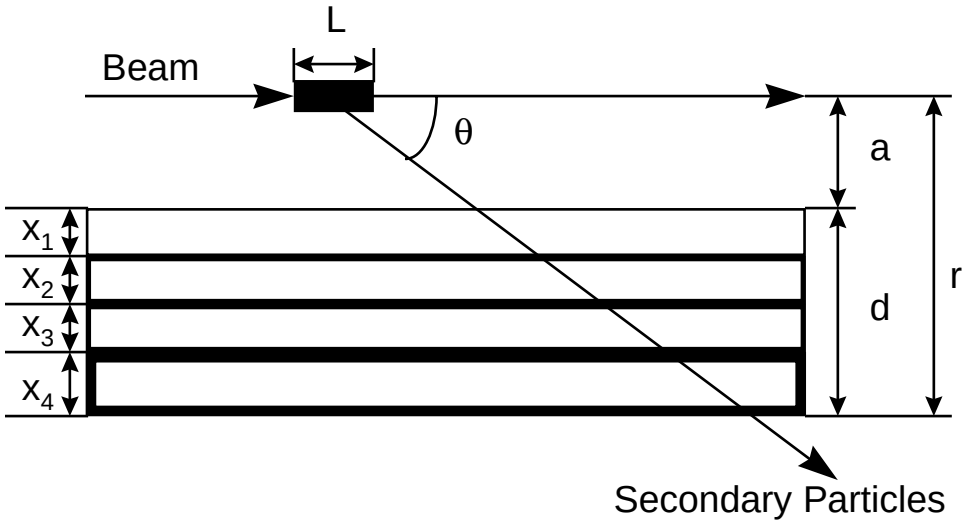

Fig. 4.21 Sketch of the geometry for the empirical Moyer Model. The proton beam, N_p impinges on the target of length L. The shield materials represented by the layers x_i, could be, for example, iron, concrete, earth and air respectively. a is the internal radius of the tunnel. The observer is situated at a radial thickness of d equal to the sum of the thicknesses of the four layers.

The number of neutrons, dN/dE which are emitted into a given element of solid angle $d\Omega$ at angle θ relative to a target struck by N_p protons in an energy interval $E + dE$ is given for a single shield material of thickness d by:

$$\frac{dN}{dE} = N_p B(E)\left(\frac{d^2Y}{dEd\Omega}\right)d\Omega \exp\left(-\frac{d\csc\theta}{\lambda(E)}\right), \qquad (4.30)$$

where *B(E)* is a "buildup factor" and the exponential function accounts for the attenuation of the radiation field by shielding of thickness, *d*, at the angle θ. The energy-dependent interaction length is denoted by $\lambda(E)$. The role of the double differential of the yield is obvious. In the above, the flux density at coordinates (r,θ) can be obtained by including the factor:

$$\frac{d\Omega}{dA} = \frac{1}{(a+d)^2 \csc^2\theta} = \frac{1}{r^2 \csc^2\theta} = \frac{1}{r'^2}. \tag{4.31}$$

The total flux density, ϕ, at the point where the ray emerges from the shield is given by

$$\phi = \frac{N_p}{r'^2}\int_{E_{\min}}^{E_{\max}} dE \;\; \frac{d^2Y}{dEd\Omega} B(E) \exp\left(-\frac{d\csc\theta}{\lambda(E)}\right). \tag{4.32}$$

Moyer introduced the following simplifying assumptions:

A. $\lambda(E) = \lambda$ = constant for $E \geq 150$ MeV and $\lambda(E) = 0$ for $E < 150$ MeV. This is a simplified rendering of the leveling-off of the inelastic cross section at high energy. Thus,

$$\phi(E_n > 150 \text{ MeV}) = \frac{N_p}{r'^2}\exp\left(-\frac{d\csc\theta}{\lambda}\right)\int_{150\text{MeV}}^{E_{\max}} \frac{d^2Y}{dEd\Omega} B(E)dE\,. \tag{4.33}$$

B. The neutrons emitted at angle θ can be represented by a simple function $f(\theta)$ multiplied by a multiplicity factor $M(E_{max})$ that depends only on the incident energy, thus:

$$\phi(E_n > 150 \text{ MeV}) = \frac{N_p}{r'^2}\exp\left(-\frac{d\csc\theta}{\lambda}\right) M(E_{\max}) f(\theta) = \frac{N_p}{r'^2}\exp\left(-\frac{d\csc\theta}{\lambda}\right) g(E_{\max},\theta) \tag{4.34}$$

where $g(E_{\max},\theta)$ is an angular distribution function that is constant for a given value of $E_{\max}$ and for a particular target.

C. The dose equivalent per fluence, *P*, for neutrons is not strongly dependent on energy over a rather wide energy range near $E \approx 150$ MeV (see Fig. 1.5). Thus the dose equivalent just outside of the shield due to neutrons with $E > 150$ MeV can be taken to be $H_{150} \approx P_{150}\,\phi(E_n > 150 \text{ MeV})$, where P_{150} is the value of this conversion factor at 150 MeV.

The total dose equivalent, *H*, is, then, given by

$$H = kH_{150} \quad \text{where} \quad k \geq 1. \tag{4.35}$$

This implicitly assumes that the low-energy neutrons are in equilibrium with those with $E > 150$ MeV so that the spectrum no longer changes with depth. This is a valid assumption for a shield more than a few mean free paths thick. Thus, Moyer's assumptions lead to

$$H = \frac{kP_{150}N_p g(E_{\max},\theta)}{(a+d)^2 \csc^2\theta} \exp\left(-\frac{d\csc\theta}{\lambda}\right). \tag{4.36}$$

One can generalize the results for the geometry shown in Fig. 4.21 with multiple materials in the shield. The parameter ζ, which replaces the ratio d/λ in the argument of the exponential function in Eq. (4.36), is introduced to take care of the *n* multiple shielding components;

$$\zeta = \sum_{i=1}^{n} \frac{x_i}{\lambda_i}, \tag{4.37}$$

where the sum is over the *n* layers of shielding. Stevenson et al. (St82) and Thomas and Thomas (Th84), have determined from global fits to data over a wide domain of energy that $f(\theta)$ is given by

$$f(\theta) = \exp(-\beta\theta), \tag{4.38}$$

where θ is in radians and β is in radians^{-1}, and that in fact, $\beta \approx 2.3$ rad^{-1} (for $E_n > 150$ MeV) for proton kinetic energies above a few GeV. Thus,

$$H = \frac{H_o(E_p)\exp(-\beta\theta)\exp(-\zeta\csc\theta)}{(r\csc\theta)^2} \tag{4.39}$$

$$\text{in which} \quad r = a + \sum_{i=1}^{n} x_i \tag{4.40}$$

and where the value of $H_o(E_p)\exp(-\beta\theta)$ is determined from the yield data and empirical measurements. $H_o(E_p)$ is best fit as a power law; $H_o(E_p) = kE^n$. From such results, per incident proton:

$$H_o(E_p) = [(2.84 \pm 0.14) \times 10^{-13}]\, E_p^{(0.80 \pm 0.10)} \qquad (\text{Sv m}^2)$$

$$= 2.84 \times 10^{-8}\, E_p^{0.8} \ (\text{mrem m}^2) = 2.8 \times 10^{-4}\, E_p^{0.8} \ (\text{mrem cm}^2), \tag{4.41}$$

with E_p in GeV. These results are derived for relatively "thick" targets (like accelerator magnets) in tunnel configurations. Schopper et al. (Sc90), based on Monte Carlo results gives values for "thin" targets of $k = 2.0 \times 10^{-14}$ (Sv m^2) and $n = 0.5$. A beam pipe would be an example of a "thin" target. The variations thus reflect buildup in the shower. For thick lateral shields close to the beam where the cascade immediately becomes fully developed and self-shielding arises, $k = (6.9 \pm 0.1) \times 10^{-15}$ (Sv m^2) and $n = 0.8$ independent of target material (Sc90 and St87).

Similarly, recommended values of λ for concrete and other materials as a function of mass number A are:

concrete: 1170 ± 20 kg m^{-2} $= 117$ g cm^{-2}

others: $428A^{1/3}$ kg m^{-2} $= 42.8A^{1/3}$ g cm^{-2}.

These values are 15-30% larger than the high energy nuclear interaction lengths (Table 1.2) and are reflective of the shower phenomena illustrated by the one-dimensional Lindenbaum model.

If one sets the partial derivative, $\partial H / \partial \theta$, equal to zero, one can derive an equation for determining the value of $\theta = \theta'$ at which the maximum dose equivalent occurs. Generally this equation can be solved by successive approximation methods,

$$\zeta \cos\theta' - \beta \sin^2 \theta' + 2\cos\theta' \sin\theta' = 0. \qquad (4.42)$$

One can substitute into the above equation to get the maximum dose equivalent at a given radial depth. According to McCaslin (McC87), with r in meters and over a wide range of values of ζ, the following holds:

$$H_{\max} = 1.66 \times 10^{-14} E_p^{0.8} \exp(-\zeta) \frac{\zeta^{0.245}}{r^2} \quad \text{(Sv per incident proton).} \qquad (4.43)$$

For values of $\zeta > 2$, the following is an equally accurate approximation:

$$H_{\max} = 1.26 \times 10^{-14} E_p^{0.8} \frac{\exp(-1.023\zeta)}{r^2} \quad \text{(Sv per incident proton).} \qquad (4.44)$$

4.6.4 The Moyer Model for a Line Source

The model discussed in Section 4.6.3 can be extended to a line source. Assume a uniform source of one proton interacting per unit length. Then, the dose equivalent from the individual increments along the line source contribute to the total at any given point, P, external to the shield. Fig. 4.22 shows the integration variables.

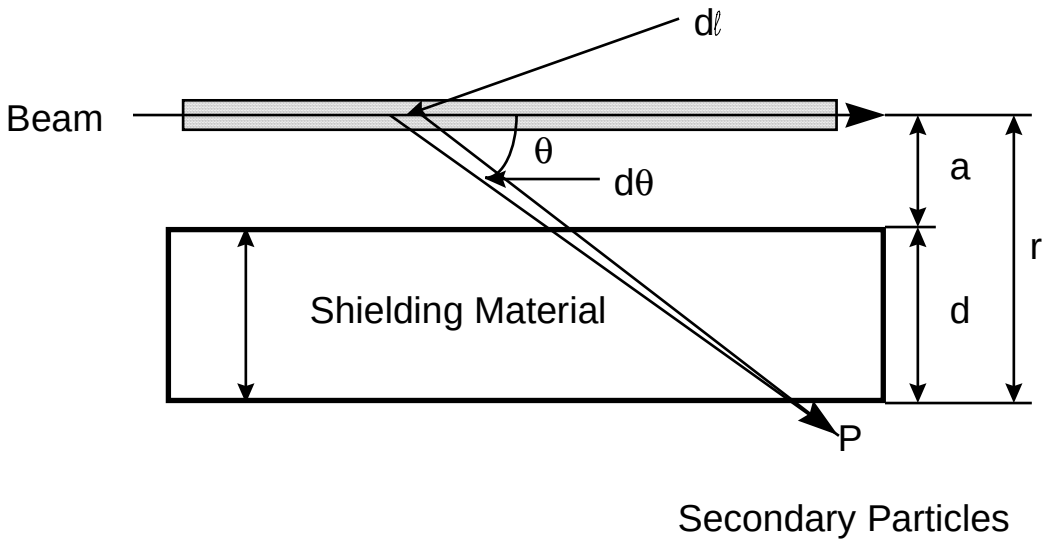

Figure 4.22 Variables of integration of Moyer point source result needed to obtain Moyer line source results.

One can integrate the elements $d\ell$ of a line source at given perpendicular distance r as follows. Making the change of variable of integration from the line integral the integral over angle θ, $d\ell = r\csc^2\theta d\theta$;

$$H = H_0\left(E_p\right)\int_{-\infty}^{\infty} d\ell \frac{\exp(-\beta\theta)\exp(-\zeta\csc\theta)}{r^2\csc^2\theta} =$$

$$H_0\left(E_p\right)\int_0^{\pi} d\theta r\csc^2\theta \frac{\exp(-\beta\theta)\exp(-\zeta\csc\theta)}{r^2\csc^2\theta} =$$

$$\frac{H_0\left(E_p\right)}{r}\int_0^{\pi} d\theta \exp(-\beta\theta)\exp(-\zeta\csc\theta) = \frac{H_0\left(E_p\right)}{r}M(\beta,\zeta)$$

(per interacting proton per unit length). (4.45)

The integral in the above, $M(\beta,\zeta)$, is known as the **Moyer integral**. The values of this integral have been tabulated by Routti and Thomas (Ro76). In view of the results found empirically for point sources, $M(2.3,\zeta)$ has obvious special significance and is tabulated extensively by, e.g., Schopper et al. (Sc90). Tesch (Te83) made an important contribution in that he determined an approximation to this integral that has become known as the **Tesch approximation**:

$$M_T(2.3,\zeta) = 0.065\exp(-1.09\zeta). \quad (4.46)$$

For "intermediate" values of ζ, $M_T(2.3,\zeta)$ can be used instead of $M(2.3,\zeta)$ to simplify calculations. Table 4.5 gives the ratio $M_T(2.3, \zeta) / M(2.3, \zeta)$ as a function of ζ. Of course, few so-called "line sources" are actually infinite in length. Thus, the integration can be limited to a finite angular range. Likewise, only a limited angular range (and hence length) contributes significantly to the Moyer integral. Tables 4.6 and 4.7 give angular integration limits (in degrees) corresponding to 90 % of the $M(2.3,\zeta)$ as a function of ζ (Table 4.6) and the distances along the *z*-axis corresponding to 90 % of $M(2.3,\zeta)$ as a function of the radial distance and ζ (Table 4.7). These calculations were done for concrete shields. McCaslin (McC85) demonstrated that the Moyer Model approach is also effective for moderately energetic heavy ions. It has also been found that the Moyer Model approach works well even into the intermediate energy region $200 < E_o < 1000$ MeV. This may be interpreted as due to the relatively smooth dependence of neutron yield upon incident proton kinetic energy. The Moyer Model generally does not work at forward angles. For these situations, the Boltzmann equation must be solved. Monte Carlo calculations are often the best approximation to such solutions.

Table 4.5 Values of the Ratio $M_T(2.3,\zeta)/M(2.3,\zeta)$ as a function of ζ. [Adapted from (Sc90).]

ζ	$M_T(2.3,.\zeta)/M(2.3/\zeta)$	ζ	$M_T(2.3,.\zeta)/M(2.3/\zeta)$
0.2	0.27	11	1.02
1	0.53	12	0.99
2	0.75	13	0.95
3	0.90	14	0.91
4	1.00	15	0.86
5	1.06	16	0.82
6	1.09	17	0.78
7	1.10	18	0.73
8	1.10	19	0.69
9	1.08	20	0.65
10	1.06		

Table 4.6 Angular integration limits in θ (degrees) which contain 90% of the Moyer Integral $M(2.3,\zeta)$. [Adapted from (Sc90).]

ζ	Lower Limit	Upper Limit	ζ	Lower Limit	Upper Limit
2.5	31.52	106.58	12	57.25	106.29
3	24.35	107.15	13	58.45	106.04
4	39.00	107.64	14	59.74	105.78
5	42.67	107.73	15	60.66	105.54
6	45.77	107.66	16	61.49	105.29
7	48.51	107.48	17	62.34	105.04
8	50.69	107.28	18	63.22	104.80
9	52.7	107.04	19	64.08	104.54
10	54.34	106.79	20	64.63	104.30
11	56.07	106.54			

Table 4.7 Distances corresponding to 90% limits in Moyer Integrals. [Adapted from (Sc90).]

Radial Distance (m)	Thickness (concrete) (meters)	Thickness (concrete) ζ	Upstream Limit, z_1 (meters)	Downstream Limit, z_2 (meters)	Total Length z_2-z_1 (meters)
1.5	0.5	1.0	-4.2	0.3	4.5
2.0	1.0.	2.0	-3.7	0.6	4.3
3.5	2.5	5.0	-3.8	1.1	4.9
6.0	5.0	10.0	-4.3	1.8	6.1
8.5	7.5	15.0	-4.8	2.4	7.2
11.0	10.0	20.0	-5.2	2.8	8.0

4.7 The Use of Monte Carlo Shielding Codes for Hadronic Cascades

4.7.1 Examples of Results of Monte Carlo Calculations

It should be quite obvious by now an approach based upon the Moyer Model is of diminished utility for beamline and shielding figures of significant complexity. Geometrical complexity presents severe limitations. The inclusion of magnetic fields is not possible. Further, the model is not valid at forward angles and for kinetic energies lower than a few hundred MeV. It is also incapable of handling the production of other types of particles aside from neutrons that can, in some cases, be copiously produced at forward angles. The treatment of labyrinth penetrations by this means is also severely limited. It also does not readily allow for calculating residual activities. Thus, the Monte Carlo technique has become a very vital tool to use in such work. Appendix A describes a number of Monte Carlo programs that have been developed at various laboratories for a variety of purposes. In this section, methods of using results from such computations are reviewed.

The code HETC remains a sort of benchmark on all of the others. A simple example of the results of a calculation performed using this code is shown in Fig. 4.23 taken from Alsmiller's results (AL75) for 200 MeV protons incident on "thin" and "thick" aluminum targets. It is a plot of r^2H as a function of angle for several intervals of θ in a concrete shield of cylindrical shape, with the beam directed down the axis of the cylinder.

For higher energies, CASIM and FLUKA have also served the role as benchmark programs. The former was developed as a very "fast" code in terms of computational speed while the latter includes the details of more physical effects. Representative results for solid iron and concrete cylinders bombarded by protons of various energies are provided in Figs. 4.24, 4.25, and 4.26. These values allow one to estimate the dose equivalent per incident proton at various locations and for various proton beam energies. They are also useful for obtaining a quick understanding of the effects of a beam absorber. Detailed calculations should be performed to assure adequately accurate designs.

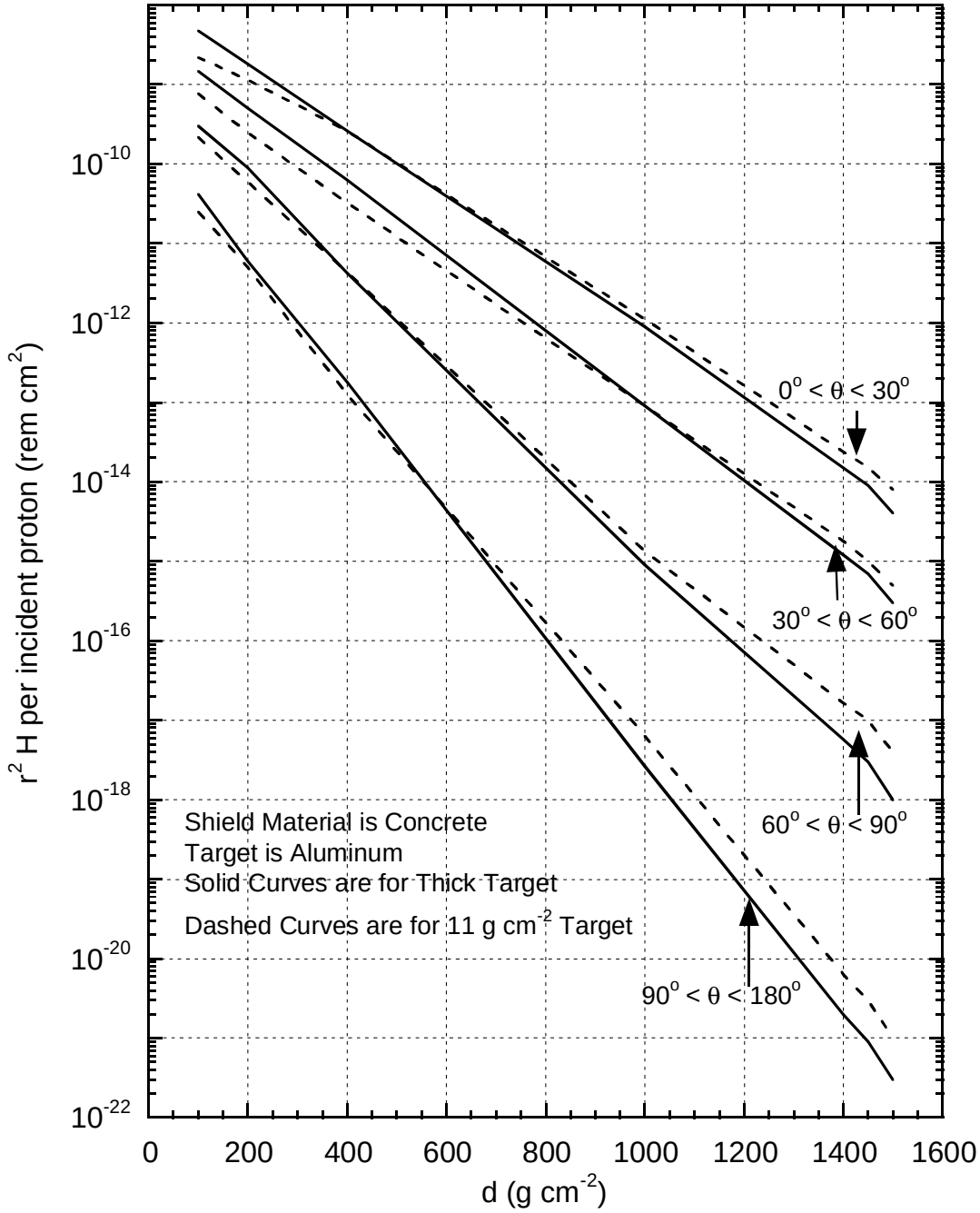

Fig. 4.23 HETC calculations of r^2H as a function of CONCRETE shield thickness, d, averaged over several intervals of θ for 200 MeV protons incident on an aluminum target. [Adapted from (Al75).]

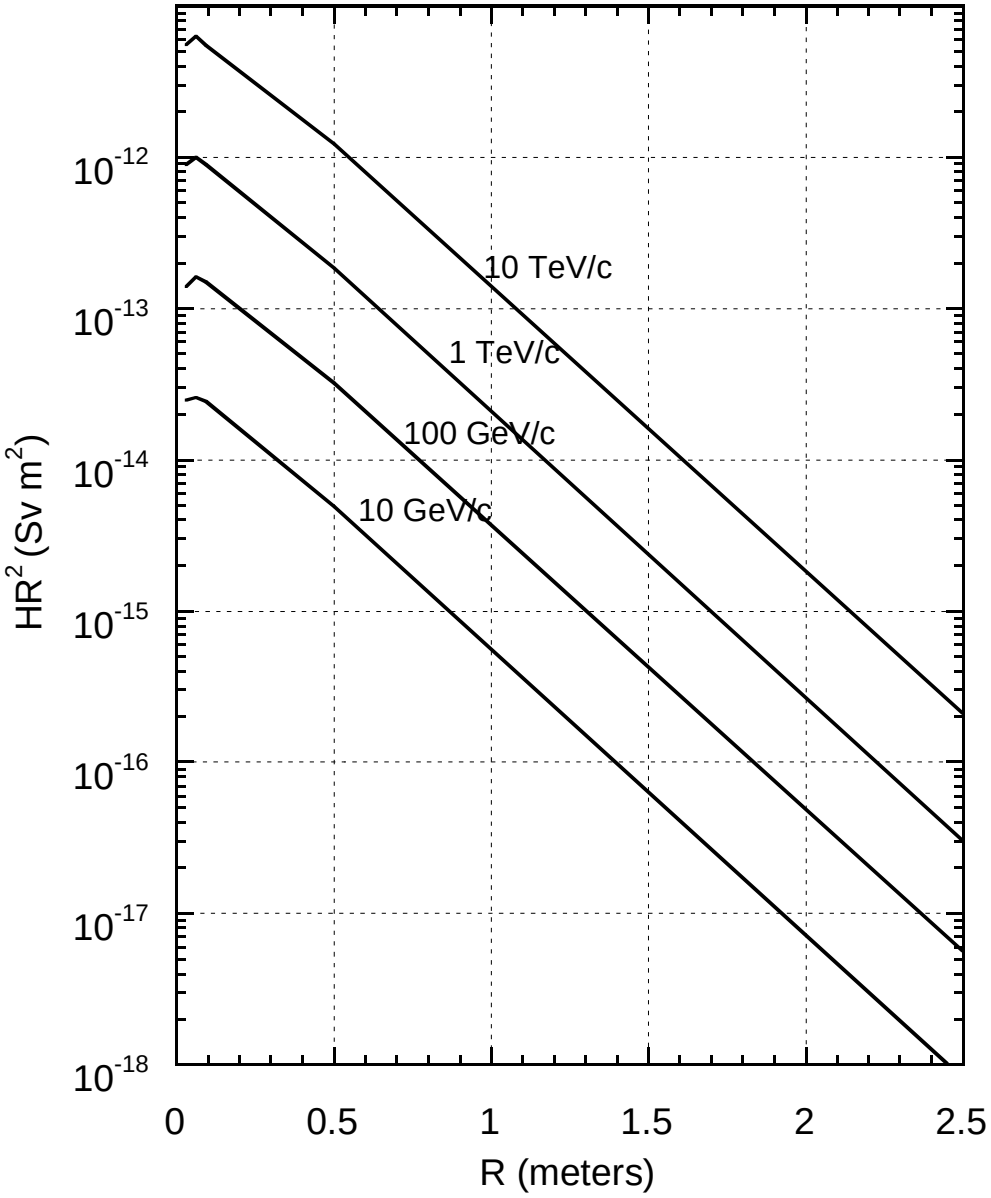

Fig. 4.24 Variation of the dose equivalent per proton at the position of the longitudinal maximum multiplied by the square of the radius HR^2 versus radius, R, for proton-induced cascades in IRON of density 7.2 g cm^{-3}. The results are fits to calculations obtained using FLUKA and MARS. [Adapted from (Sc90).]

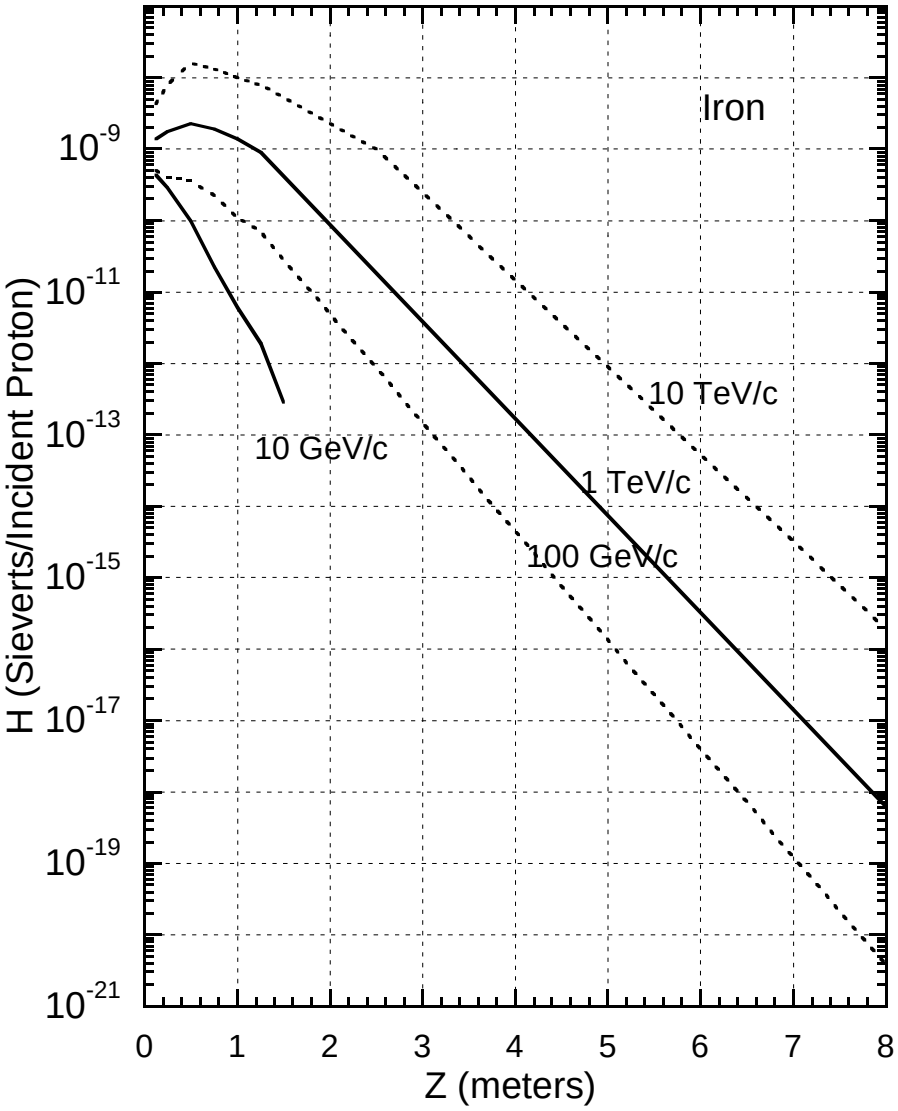

Fig. 4.25 Variations of the dose equivalent per proton, *H*, on the longitudinal axis vs. depth *Z* in the shield for proton-induced cascades in IRON of density 7.2 g cm^{-3}. The curves are the result of CASIM calculations for incident proton momenta of 100 GeV/c, 1 TeV/c, and 10 TeV/c and FLUKA results for 10 GeV/c. [Adapted from (Sc90).]

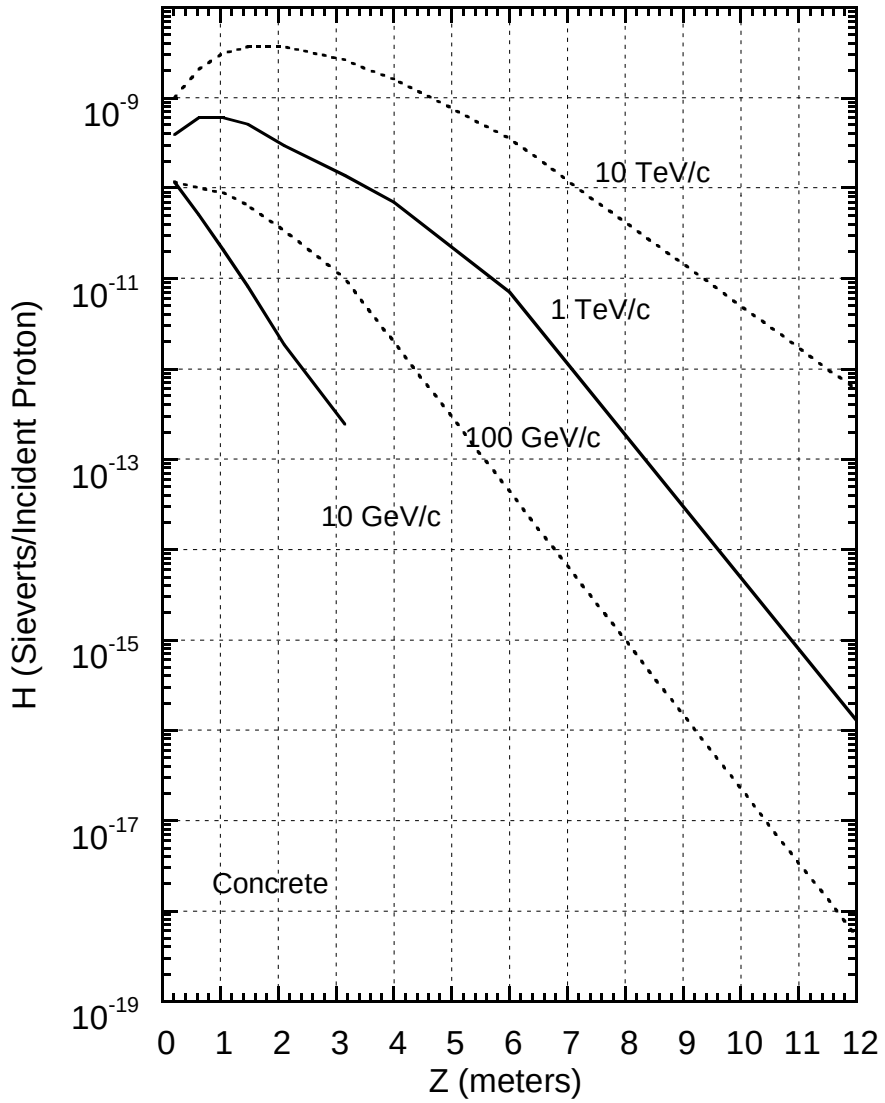

Fig. 4.26 Variations of the dose equivalent per proton, *H*, on the longitudinal axis vs. depth *Z* in the shield for proton-induced cascades in CONCRETE of density 2.4 g cm^{-3}. The curves are the result of CASIM calculations for incident proton momenta of 100 GeV/c, 1 TeV/c, and 10 TeV/c and FLUKA results for 10 GeV/c. [Adapted from (Sc90).]

4.7.2 General Comments on Monte Carlo Star-to-Dose Conversions

All of the above codes, in general, calculate **star densities** as their most basic output quantity. This quantity, generally denoted by *S*, is more correctly called the density of inelastic interactions (stars cm^{-3}) and is relatively easy to tabulate as the calculation proceeds since only a simple counting process is involved. The term "star" comes from historic cosmic ray work in which the high energy interaction events, with their large

multiplicities, appeared as tracks originating from a point. In a shield comprised of more than one material, the star density may change dramatically from one material boundary to the other, reflective of differing material densities and atomic number. A related quantity is the **star fluence**, denoted by ϕ_S, the product of the star density and the nuclear interaction length. The star fluence roughly corresponds to the fluence of hadrons having energies above that where the cross section "levels off" and is reflective of any "artificial" thresholds in the calculation. In contrast to the situation found with star density, due to continuity, the star fluence is conserved across material boundaries.

The **dose equivalent per star density conversion factor** is a rather important ingredient of radiation protection calculations. Perhaps the best results have been provided by Stevenson (St86). While this conversion factor is somewhat dependent upon the position in the shield, after a shield thickness sufficient to establish "equilibrium" spectra, a constant value may be used for high energy protons (i.e., $E_{proton} > 1$ GeV) , and other hadrons, within a given material. In other words, the energy and spatial dependences are rather weak. These values for these quantities, as well as the related **dose equivalent per star fluence conversion factors**, are given in Table 4.8.

Table 4.8 Coefficients to convert star densities, *S*, and star fluence, ϕ_S, into dose equivalent. A star density is transformed into the corresponding star fluence by the relation $\phi_S = S\lambda$ where λ is the nuclear interaction length. [Adapted from (St86).]

Proton Energy (GeV)	Absorber Material	Dose Equivalent/Star Density (Sv cm^3/star) (x 10^{-8})	λ (cm)	Dose Equivalent/Star Fluence (Sv cm^2/star) (x 10^{-9})
10	Iron[a]	2.04 $\pm$ 0.06	17.1	1.19 $\pm$ 0.04
100	Iron[a]	2.15 $\pm$ 0.08	17.8	1.21 $\pm$ 0.05
1000	Iron[a]	2.12 $\pm$ 0.08	17.2	1.23 $\pm$ 0.05
Mean	Iron[a]	2.10 $\pm$ 0.04		1.21 $\pm$ 0.02
100	Aluminum	4.62 $\pm$ 0.17	38.6	1.20 $\pm$ 0.04
100	Tungsten	1.19 $\pm$ 0.05	9.25	1.29 $\pm$ 0.05
	Concrete	4.9	40.0	1.22
Mean	All			1.22 $\pm$ 0.02

[a]As discussed in detail in Section 6.3.5, iron shielding presents a unique problem due to the copious emission of low energy neutrons in shields of modest thickness. The values reported here are for relatively thin iron shields of only one or two mean free paths. If a thick iron shield is encountered that is not "finished" with at least 50 cm, or so, of concrete as the outermost layer, one should multiply these conversion factors by a factor of approximately 5.

Compilations of such calculations have been given by Van Ginneken (Va75 and Va87) and by Cossairt (Co82b). Schopper et al. (Sc90) have also compiled a comprehensive set of Monte Carlo results. A convenient way to display these results is to provide contour plots of star density as function of longitudinal coordinate, *Z*, and radial coordinate, *R*,

assuming cylindrical symmetry. Appendix B provides examples of the results of such hadronic Monte Carlo calculations that are meant to illustrate a number of situations commonly encountered. One of the salient advantages of the Monte Carlo method is the ability to handle configurations of arbitrary complexity and results for both solid cylinders and more complicated configurations are provided in Appendix B.

4.7.3 Shielding Against Muons at Proton Accelerators

The production of muons has been discussed previously in Section 4.2.4. At the higher energies, there are significant complications in that muon creation mechanisms, in addition to pion and kaon production and subsequent decay, are possible. However, the muons from pion and kaon decay generally, but not universally, represent the most important consideration in practical shielding calculations. In Monte Carlo calculations, it is straightforward to "create" muons and follow them through the shielding medium. Muon transport is well understood, as discussed in the preceding chapters.

The particle energy downgrades quickly in hadronic showers so the most penetrating muons must originate in the first few generations of the process. These energetic muons are not distributed over a large volume of space as are the neutrons. However, geometric effects or deflections by magnetic fields encountered near the point of production can affect the muon fluence at large distances. Thus, the presence of large "empty" spaces, that is, decay paths (vacuum or air) near the point of interaction provide opportunity for the pions or kaons to decay into muons before they can be removed by nuclear interactions in solid materials. This is particularly important for the typical situation of a target used to produce secondary beams followed (downstream) by an air or vacuum gap (the space for decay into muons) and then a beam dump. If magnetic fields are present, the muon fluence generally peaks in the bend plane. Multiple Coulomb scattering from nuclei is an important effect in muon transport.

Generally the most copious sources of muons are those due to the decay of pions and kaons. There are several important facts about such muons that are summarized below:

A. The decay lengths (mean length for π or K to decay), Λ, are:

$\Lambda_\pi = 55.9p$ (meters), where p is the pion momentum in GeV/c, and
$\Lambda_K = 7.51p$ (meters), where p is the kaon momentum in GeV/c.

The decay length can be used to estimate the total number of muons present. For example, a beam of 10^7 pions at 20 GeV/c will decay in a distance of 50 meters into 10^7 x [50 meters]/[56 x 20 meters decay length] = 4.5 x 10^5 muons. This uses the fact that the path length (50 meters) is small compared with the mean decay length of 1120 meters. If the path length, x, was comparable to the decay length, Λ, the intensity of 10^7 would be multiplied by the exponential factor $\{1 - \exp(x/\Lambda)\}$.

B. If $\beta \approx 1$, relativistic kinematics determines that the ratio, k_i, of the *minimum* momentum of the daughter muon ($p_{\min}$) to the momentum of the parent pion or kaon (p_i) is given by

$$k_i = p_{\min}/p_{\text{parent}} = (m_\mu/m_{parent})^2 \, . \qquad (4.47)$$

The result is that k_i has a value of 0.57 for muons with pion parents and 0.046 for muons with kaon parents. Thus if, say, a beam transport system restricts the momentum of pions to some minimum value, then the momentum of the decay muons has a minimum value given by the above.

C. Since in the center of mass frame of reference the decay is isotropic, and there is a one-to-one relationship between the muon momentum and the angle of emission, for muon momenta >> m_{parent} (in units where c = 1) the momentum spectrum of the muons can be expressed as

$$\frac{dN}{dp} = \frac{1}{p_{parent}(1-k_i)} \quad . \qquad (4.48)$$

This means that the spectrum of daughter muons uniformly extends from the momentum of the parent down to the minimum established in Eq. (4.47).

D. Relativistic kinematics also gives the result that the maximum angle, in the laboratory frame of reference, between the momentum vector of the muon and that of the parent particle is given by

$$\tan\theta_{\max} = \frac{(m_{parent}^2 - m_\mu^2)}{2\,p_{parent} m_\mu} . \qquad (4.49)$$

For muons originating from pion decay, θ_{max} is at most several milliradians. However, for muons originating from the decay of 5 GeV kaons, θ_{max} is a relatively large 12°. Thus $\pi -> \mu$ decays can be assumed to be collinear while $K -> \mu$ decays have significant divergence at the lower energies.

Monte Carlo calculations are needed to adequately describe the production and transport of muons because of the sensitivity to details of the geometry that determine the pion and kaon flight paths and influence the muon populations. Schopper et al, (Sc90) has presented some useful information about the production of muons that one can use to make approximate estimates by giving calculated values of angular distributions of muon spectra with an absolute normalization from pion and kaon decays for one meter decay paths. Neither the effects of absorbers nor magnetic fields are included in these results. For other decay paths that are short compared with the decay length, one can simply scale by the length of the actual decay path. The results are displayed in Fig. 4.27.

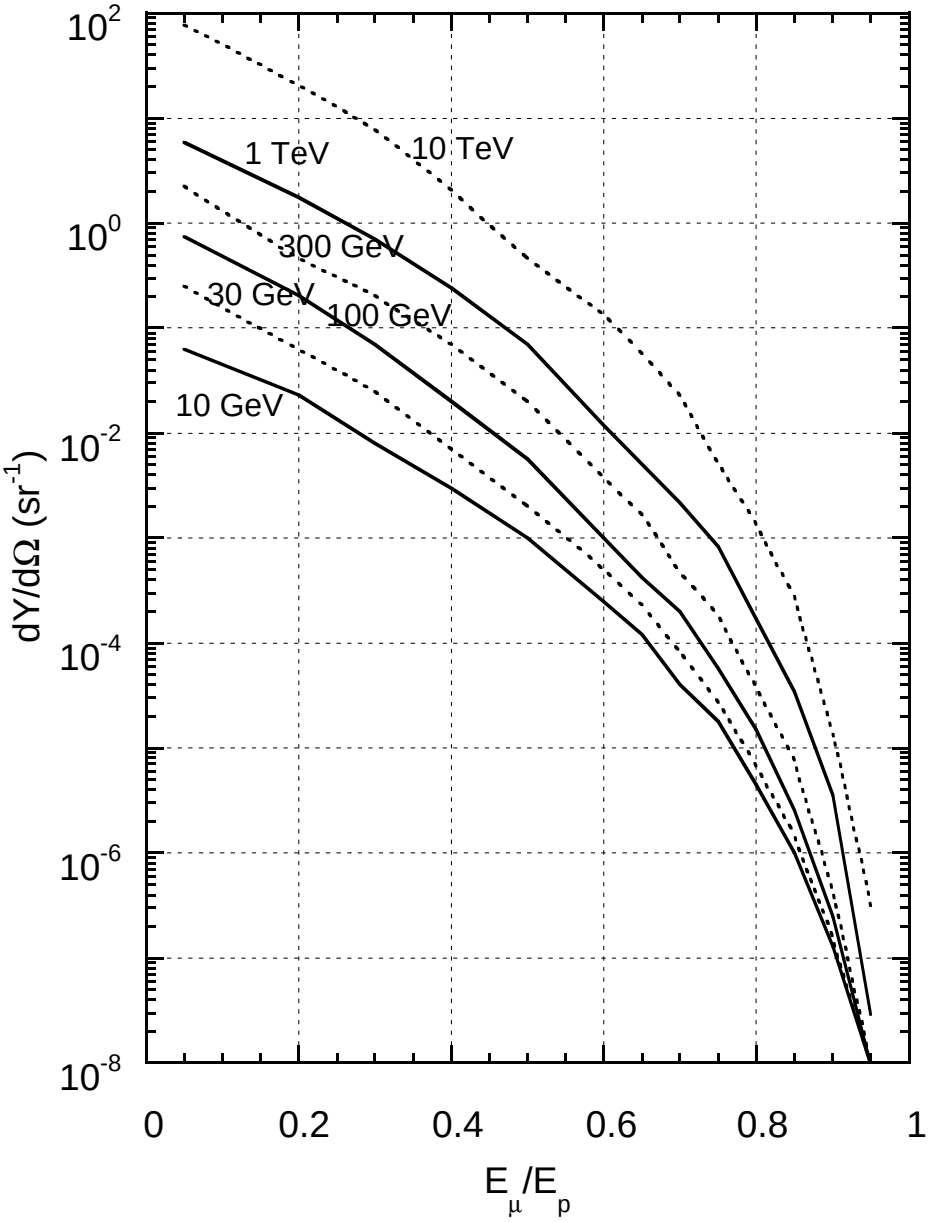

Fig. 4.27 Yield of muons from the decay of pions and kaons of both charges produced in proton-Fe collisions at several energies of the incident proton. The distance available for decay (the decay path) is assumed to be 1 meter. The abscissa, E_μ/E_p is the muon energy expressed as a fraction of the incident proton energy. The ordinate, $dY/d\Omega$, is the number of muons having an energy greater than E_μ, per incident proton sr^{-1}. All values are for $\theta = 0$. [Adapted from (Sc90).]

Decays of other particles can be important sources of muons at higher energies, especially those found in hadron-hadron collisions at high energy colliders. Especially notable are those from charm (D) and bottom (B) meson decays (Sc90). The muons from these sources are often called "direct" muons due to the short lifetimes and decay lengths involved. The masses of these parent particles and their mean lives, τ, are as follows:

$m(D^{\pm}) = 1869.3 \pm 0.5$ MeV, $\tau = (10.66 \pm 0.23) \times 10^{-13}$ s, $c\tau = 320$ μm,
$m(B^{\pm}) = 5278.6 \pm 2.0$ MeV, $\tau = (12.9 \pm 0.5) \times 10^{-13}$ s, $c\tau = 387$ μm.

Figures 4.28 and 4.29 give results for muons originating from these decays.

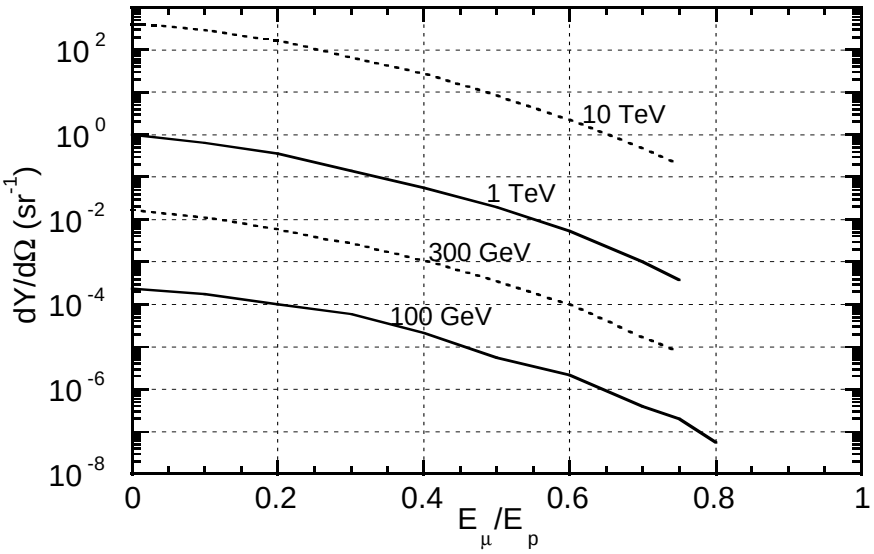

.

Fig. 4.28 Muons from the decay of D-mesons produced in proton-proton collisions at four incident proton energies and at θ = 0. The abscissa, E_μ/E_p is the muon energy expressed as a fraction of the incident proton energy. The ordinate, $dY/d\Omega$, is the number of muons per unit solid angle per incident proton having an energy greater than E_μ, expressed in sr^{-1}. [Adapted from (Sc90).]

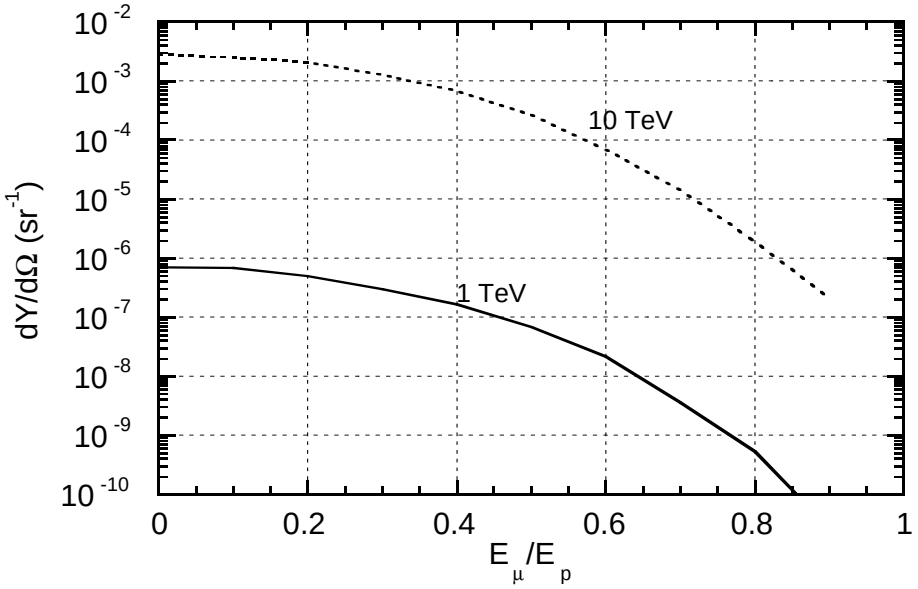

Fig. 4.29 Muons from the decay of B-mesons produced in proton-proton collisions at various energies of the incident proton and at $\theta = 0$. The abscissa, E_μ/E_p is the muon energy expressed as a fraction of the incident proton energy. The ordinate, $dY/d\Omega$, is the number of muons per unit solid angle per incident proton having an energy greater than E_μ, expressed in sr^{-1}. [Adapted from (Sc90).]

An approximate method for calculating muon flux densities at proton accelerators has been developed by Sullivan (Su92) based upon a semi-empirical fit to existing muon production data. Sullivan gives an equation for the flux density of muons per meter of decay path as a function of shield thickness found along the proton beam axis (that is, on the straight-ahead maximum of the muons):

$$\Phi = 0.085 \frac{Ex}{X^2} \exp\left\{-\frac{\alpha\, t}{E}\right\}, \tag{4.50}$$

where Φ is the fluence (muons m^{-2}) per interacting proton, E is the proton beam energy (GeV), X is the distance of the point of concern to the point of production of the pions and kaons (meters), x is the average path length (i.e., the decay path) of the pions and kaons in air, gases, or vacuum prior to their absorption by solids or liquids, and α is an effective average energy loss rate (GeV $meter^{-1}$) for the muons in a shield of thickness t (meters). Values of α for typical shielding materials are provided in Table 4.9. x can be taken to be the actual physical length of the decay path, or according to Sullivan, for a beam dump situation, x can reasonably be taken to be 1.8 times the hadron nuclear interaction mean free path for the material comprising the beam dump. It is obvious that the argument of the exponential in Eq. (4.50) can be expanded as the sum over the materials comprising a composite shield. Sullivan has also given a prescription for

calculating the full width at half maximum (FWHM) of the muon distribution at the boundary of such a shield. This is given by:

$$FWHM = 4.6\frac{X}{\sqrt{\alpha E t}} \text{ (meters).} \qquad (4.51)$$

Table 4.9 Values of α for typical shielding materials for use in Eqs (4.50) and (4.51) according to Sullivan (Su92).

Material	α (GeV m^{-1})	Density, ρ (g cm^{-3})
Concrete[a]	9.0	2.35
Water	4.0	1.0
Iron	23.0	7.4
Lead	29.0	11.3

[a]The value for concrete can be used for earth if one adjusts it to the correct density.

Problems

1. One can use measurement results to check Sullivan's formula, Eq. (4.4), for hadron fluence above 40 MeV for high-energy proton interactions. Check the agreement for the 22 and 225 GeV/c data in Figs. 4.7 and 4.8 for 3 representative angles at one meter. (Ignore the fact that the formula is for hadrons > 40 MeV while the only data provided is for hadrons >35 MeV and 50 MeV, but do not ignore the difference between normalizing to incident versus interacting protons.) (It is valid to make the comparison on yield per interacting proton since the results in Fig. 4.8 is for targets approximately 1 interaction length long.) Comment on the quality of the agreement.

2. Calculations can also be used to check the Tesch curve for dose equivalent at θ = 90º (Fig. 4.10). Use the 200 MeV calculations in Fig. 4.4 to do this by crudely numerically integrating the $60^o < \theta < 90^o$ yields to determine the average energy of the neutrons and the total fluence at $\theta = 90^o$ and at 1 meter. Use the results along with dose equivalent per fluence curves to obtain the dose equivalent per proton to compare with Tesch's result. (Iron is considered equivalent to copper for this problem.)

3. A copper target at an accelerator is struck by 1 μA of 100 MeV protons.

   a) Use Tesch's curve in Fig. 4.10 to calculate the dose equivalent rate at 2 m and θ = 90º relative to this target.

   b) Compare this result with the neutron dose equivalent rate calculated in Chapter 3, problem 5 for an electron accelerator having the same intensity and beam energy and discuss. (Scale the relevant result of Chapter 3, problem 5 by the appropriate yield for copper versus tungsten.)

4. It is often necessary to work from fragmentary data to determine other quantities.

   a) Use McCaslin's results, Eq. (4.14), and the appropriate dose equivalent/fluence to calculate the dose equivalent rate at 1 meter and at θ = 30º for a target struck by 10^8 670 MeV/amu ^{20}Ne ions per sec. (Hint: Use all available spectrum information.)

   b) Use McCaslin's results to obtain the total yield of neutrons per ion with E_n > 6.5 MeV. Assuming the target to be iron or copper, how does this yield correspond to that due to 700 MeV protons? Do this for both E_n > 6.5 MeV and E_n > 20 MeV to understand the overall composition. Hint: Integrate over the unit sphere (double integral over spherical coordinates θ & ϕ).

The following indefinite integrals are needed:

$$\int \frac{dx \sin x}{x} = x - \frac{x^3}{3 \cdot 3!} + \frac{x^5}{5 \cdot 5!} - \frac{x^7}{7 \cdot 7!} + \ldots$$

$$\int e^{ax} \sin bx dx = \frac{e^{ax}[a \sin bx - b \cos bx]}{a^2 + b^2}$$

The elemental area on the sphere of radius R is $dA = r^2 \sin\theta \, d\theta d\phi$, where ϕ is the standard azimuthal coordinate in a spherical coordinate system.

5. It is asserted that if the assumption is made that the limiting attenuation is simply geometric, with the nucleon radius equal to 1.2 x 10^{-13} cm, then $\rho\lambda_{atten} = 36.7A^{1/3}$ (g cm^{-2}). Show this to be the case using the volume of a nucleus and nucleons along with the cross section.

6. a) Use the Moyer Model to calculate the dose equivalent rate (mrem/hr) lateral ($\theta = 90^o$) to a magnet centered in a 1.5 m radius tunnel. The magnet is struck by 10^{12} protons at 100 GeV (per sec). The tunnel walls consist of 1/3 m concrete followed by soil having the same composition [ρ(concrete) = 2.5 g cm^{-3}, ρ(soil) = 2.0 g cm^{-3}]. Perform the same calculation for several thicknesses of soil out to 6 meters of soil radially. Do this for increments of 1 meter from 1 meter to 6 meters of soil.

   b) Calculate the result if the same beam loss occurs uniformly over a string of such magnets 100 meters long in the same tunnel at the same soil thicknesses as above. Use the Tesch approximation. Approximately how many meters of beam loss does it take to cause 90% of the calculated dose equivalent rate at 6 m of lateral soil shield?

   c) For the point loss in part a), at what value of θ does the maximum dose equivalent rate occur and what is its magnitude outside of 6 meters of soil shield? (Use successive approximations to solve.)

7. An accelerator delivers 10^{12} 1 TeV protons per second head-on on the inner edge of a magnet. Use the CASIM calculations found in Appendix B to determine the approximate dose equivalent rate at R = 400 centimeters and compare with a result using the Moyer equation for point loss. Both calculations should be at the location of the maximum dose equivalent. Assume ρ(concrete) = 2.5 g cm^{-3} and ρ(soil) = 2.25 g cm^{-3}. Why might there be an explainable disagreement between the two results?

8. Using the results of Monte Carlo hadron calculations (FLUKA/MARS), calculate, for solid shields of iron (cylinders), what longitudinal thickness of iron is needed to achieve the same hadron dose equivalent per proton on the beam axis as found at R = 50 cm at 10 GeV/c, 100 GeV/c, 1000 GeV/c and 10 TeV/c. Use the maximum value of H (r = 50 cm).

9. In the Fig. 4.4, we have calculations of neutron energy spectra for 200 MeV protons incident on various targets, including aluminum. In Fig. 4.23, calculations of dose equivalent values for concrete shielding surrounding aluminum targets at E_p = 200 MeV are given. At shielding thicknesses approaching zero and at forward angles, are the two results in "sensible" (that is, approximate, agreement)? (Hint: "Integrate" crudely over the forward spectrum to obtain the fluence/proton and convert this fluence to dose equivalent.)

   a) Make the comparison for zero shield thickness and in the angular range $0 < \theta < 30^{o}$.

   b) Now use the shielding calculations to obtain the dose equivalent rate (rem h^{-1}) due to a 1 μA beam incident at 200 MeV on such a thick target at a distance of 4 m from the target with 0, 1, 2, & 3 m of intervening concrete shielding (ρ = 2.5 g cm^{-3}) for $\theta = 15^{o}$ and $\theta = 75^{o}$. (Hint: Use the center of the angular bins.)

10. Assume that a target is struck by 100 GeV protons and that a 10 m long decay space exists for π and K decay. Use the curves in Fig. 4.27 to crudely estimate the muon flux density and dose equivalent rates (mrem/h) at 1 km away and at $\theta = 0^{o}$ if 10^{12} protons/second are targeted in this manner if the following additional assumptions are made:

   a) Assume that there is no shielding present (neglect air scattering and in-scattering from the ground). (Hint: The muon yield for this decay space will scale with the length of the decay space.)

   b) Assume there is 100 meters of intervening shielding of earth (ρ = 2 g cm^{-3}) (Hint: use Fig. 1.9 range-energy curves to determine the mean energy of muons which will penetrate this much shielding). Neglect multiple scattering and range-straggling.

   c) If the beam operates for 4000 h yr^{-1}, is 100 mrem yr^{-1} exceeded? Will multiple scattering increase or decrease this dose equivalent? (Answer both questions for the soil-shielded case only.)

   d) Repeat Part b) of the same calculation using Sullivan's semi-empirical approach. If the disagreement between the results obtained using the two methods is large, suggest an explanation of a possible cause of the difference.